Simulation of freckles during vertical solidification of binary alloys.

— **Source link** ⎘

Sergio D. Felicelli, Juan C. Heinrich, David R. Poirier

Institutions: University of Arizona

Topics: Directional solidification

Related papers:

- A continuum model for momentum, heat and species transport in binary solid-liquid phase change systems—I. Model formulation

- Conservation of mass and momentum for the flow of interdendritic liquid during solidification

- Numerical model for dendritic solidification of binary alloys

- Permeability for flow of interdendritic liquid in columnar-dendritic alloys

- A volume-averaged two-phase model for transport phenomena during solidification

Simulation of freckles during vertical solidification of binary alloys.

Item Type	text; Dissertation-Reproduction (electronic)
Authors	Felicelli, Sergio Daniel.
Publisher	The University of Arizona.
Rights	Copyright © is held by the author. Digital access to this material is made possible by the University Libraries, University of Arizona. Further transmission, reproduction or presentation (such as public display or performance) of protected items is prohibited except with permission of the author.
Download date	31/05/2022 09:48:42
Link to Item	http://hdl.handle.net/10150/185606

INFORMATION TO USERS

This manuscript has been reproduced from the microfilm master. UMI films the text directly from the original or copy submitted. Thus, some thesis and dissertation copies are in typewriter face, while others may be from any type of computer printer.

The quality of this reproduction is dependent upon the quality of the copy submitted. Broken or indistinct print, colored or poor quality illustrations and photographs, print bleedthrough, substandard margins, and improper alignment can adversely affect reproduction.

In the unlikely event that the author did not send UMI a complete manuscript and there are missing pages, these will be noted. Also, if unauthorized copyright material had to be removed, a note will indicate the deletion.

Oversize materials (e.g., maps, drawings, charts) are reproduced by sectioning the original, beginning at the upper left-hand corner and continuing from left to right in equal sections with small overlaps. Each original is also photographed in one exposure and is included in reduced form at the back of the book.

Photographs included in the original manuscript have been reproduced xerographically in this copy. Higher quality 6" x 9" black and white photographic prints are available for any photographs or illustrations appearing in this copy for an additional charge. Contact UMI directly to order.

Simulation of freckles during vertical solidification of binary alloys

Felicelli, Sergio Daniel, Ph.D.

The University of Arizona, 1991

SIMULATION OF FRECKLES DURING VERTICAL

SOLIDIFICATION OF BINARY ALLOYS

by

Sergio Daniel Felicelli

A Dissertation Submitted to the Faculty of the

DEPARTMENT OF AEROSPACE AND MECHANICAL ENGINEERING

In Partial Fulfillment of the Requirements
For the Degree of

DOCTOR OF PHILOSOPHY
WITH A MAJOR IN MECHANICAL ENGINEERING
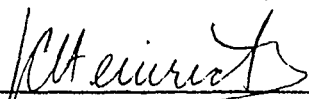
In the Graduate College
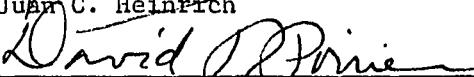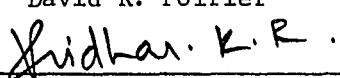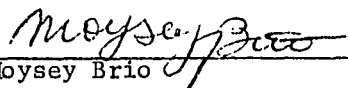
THE UNIVERSITY OF ARIZONA

1 9 9 1

THE UNIVERSITY OF ARIZONA
GRADUATE COLLEGE

As members of the Final Examination Committee, we certify that we have read

the dissertation prepared by ___Sergio Daniel Felicelli___
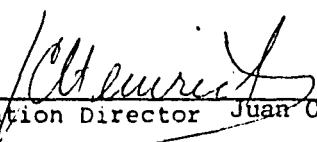
entitled ___SIMULATION OF FRECKLES DURING VERTICAL SOLIDIFICATION OF___

___BINARY ALLOYS___

and recommend that it be accepted as fulfilling the dissertation requirement

for the Degree of ___Doctor of Philosophy___ .

Juan C. Heinrich	7/24/91 Date
David R. Poirier	7/24/91 Date
R. R. Sridhar	7/24/91 Date
Moysey Brio	7/24/91 Date
	Date

Final approval and acceptance of this dissertation is contingent upon the
candidate's submission of the final copy of the dissertation to the Graduate
College.

I hereby certify that I have read this dissertation prepared under my
direction and recommend that it be accepted as fulfilling the dissertation
requirement.

___Dissertation Director Juan C. Heinrich___   ___7/24/91___ Date

STATEMENT BY AUTHOR

This dissertation has been submitted in partial fulfillment of requirements for an advanced degree at The University of Arizona and is deposited in the University Library to be made available to borrowers under rules of the Library.

Brief quotations from this dissertation are allowable without special permission, provided that accurate acknowledgment of source is made. Requests for permission for extended quotation from or reproduction of this manuscript in whole or in part may be granted by the head of the major department or the Dean of the Graduate College when in his or her judgment the proposed use of the material is in the interests of scholarship. In all other instances, however, permission must be obtained from the author.

SIGNED:_____

ACKNOWLEDGMENTS

TABLE OF CONTENTS

Page

LIST OF ILLUSTRATIONS 7

LIST OF TABLES 11

ABSTRACT 12

CHAPTER 1 - INTRODUCTION 14

    1.1   Motivation for This Work 14
    1.2   Background 15
    1.3   Experimental Observation 18
    1.4   Numerical Modeling 22

CHAPTER 2 - MATHEMATICAL MODEL 26

    2.1   Introduction 26
    2.2   Governing Equations 28
        2.2.1   Conservation of Mass and Momentum 28
        2.2.2   Conservation of Energy and Solute
                Content 32
        2.2.3   Phase Diagram Constraints 34
    2.3   Numerical Scheme 36
    2.4   Remelting 41
    2.5   Modified Energy Equation 43
    2.6   Solidification at Eutectic Temperature 45
    2.7   Nondimensionalization 49

CHAPTER 3 - NUMERICAL RESULTS 54

    3.1   Code Verification 54
        3.1.1   1-D Case with Constant Temperature
                Gradient 54

LIST OF ILLUSTRATIONS

LIST OF TABLES

ABSTRACT

The formation of channel segregates or freckles during vertical

solidification of Pb-Sn alloys is simulated. The simulation is based on a

mathematical model of dendritic solidification, in which the solid plus liquid

zone is modeled as an anisotropic porous medium of variable porosity. The

alloy solidifies from an initial melt and proceeds until the alloy is completely

solidified, and the final macrosegregation can be predicted.

The growth process is calculated by solving the fully coupled equations

of momentum, energy and solute transport, as well as by maintaining the

thermodynamic constraints dictated by the equilibrium phase diagram of the

alloy.

It is found that the thermosolutal convection that occurs during

solidification, under certain growth conditions, can produce localized

segregation zones, varying in shape from short streaks or pockets to long and

narrow channels or freckles rich in solute.

Several numerical examples show how these defects originate and why

they subsist or die, depending on whether they face a favorable or adverse convection pattern ahead of the solidification front.

The response, in both appearance and location, of channels to the variation of the cooling conditions is in good agreement with experiments, although the preference of channels to form on the outer surface of the casting, rather than in the interior, is greater than what is normally observed in Pb-Sn alloys.

A mechanism that favors the formation of freckles within the body of the casting, because of defects in the dendritic mushy zone, is proposed and illustrated numerically.

CHAPTER 1 - INTRODUCTION

1.1 Motivation for This Work

Freckles are macroscopic segregation defects that are found in many unidirectionally solidified alloys. Today's directional solidification processes can produce high performance materials, suitable for components that must operate under severe conditions of temperatures and stresses, as in the case of gas turbine blades of aero engines. A columnar microstructure, with all the grain boundaries running in the longitudinal direction of the casting, prevents the usual failures associated with grain boundaries that are transverse to the applied stress.[1]

Improper control of species transport, however, occurring by advection and diffusion during solidification, can result in localized regions of segregation with unacceptable levels of inhomogeneities. Freckling is one of the most severe types of segregation. This nonuniformity of composition reflects itself in an undesirable variation in mechanical, chemical, electrical,

magnetic or other physical properties of the alloy and thus leads to an inferior performance during service. In ingot production, an excessive number of defects can require a large amount of cropping, at a considerable cost of energy and material.

The analysis of the transport mechanisms, relevant to multiconstituent phase changes, encompasses a broad spectrum of engineering and scientific disciplines such as process metallurgy, thermodynamics, heat and mass transfer and fluid mechanics. A comprehensive approach that integrates these areas in a consistent framework is essential to predict realistic system behavior. This work is motivated by the need to control casting defects in directionally solidified materials. By explaining and illustrating why and how these defects originate, guidance in the proper specification of process parameters, as well as the further understanding of macrosegregation phenomena, are provided.

1.2 Background

When a molten alloy, initially at uniform composition, is solidified, several physical factors contribute to a final solid of nonuniform composition. First, the density of the solid and liquid phases (ρ_S and ρ_L, respectively) are

different, resulting either in liquid flow towards the freezing regions to feed shrinkage if $\rho_S > \rho_L$, or flow away from the solid liquid interface if $\rho_S < \rho_L$. Second, temperature and solute gradients develop at the solid-liquid interface because of the latent heat of fusion released during solidification. Third, in most systems the alloy components have different solubilities in the solid and liquid phases; hence the phases can become preferentially enriched or depleted of alloy elements. There is little that can be done to alter these three factors, which are dictated solely by fundamental physical and chemical laws governing the atomic or molecular arrangements in the solid and liquid states. The final solid formed is thus necessarily inhomogeneous in composition (Laxmanan et al.[2]).

It is now widely accepted, however, that none of these factors leads to severe segregation defects like freckles, but freckles are a direct consequence of a fourth factor: the gravity driven fluid flow. In multicomponent alloys, the density of the liquid varies with both temperature and concentration. Hence, natural convection can be induced by both temperature and concentration gradients present during solidification. Temperature gradients can be imposed externally or originate because of the latent heat release. Concentration gradients result from the different solubilities of the alloying elements in the liquid and solid phases. In liquid metals, as in water-base mixtures, diffusion

of energy is far more effective than diffusion of species, and the convective motion shows characteristics similar to those pertaining to double-diffusive phenomena, like plumes and finger convection, which are directly related to channel segregation.

Unlike pure substances, the freezing of alloys takes place over a range of temperatures at which the solid and liquid phases coexist in equilibrium[1], depending on the local composition. Temperature and concentration gradients at the solid/liquid interface are such that morphological instabilities cause the interface to deviate from the planar form observed in the solidification of pure substances. Rather, the solid propagates in the form of tree-like protrusions called "dendrites", forming a mixture of the interdendritic solid and interdendritic liquid in the "mushy zone", whose physical substructure has a length scale on the order of 100µm. The segregation produced by the first three factors mentioned above is generally restricted to these length scales, and is known as microsegregation. The advection of segregated solid and liquid phases that accompanies solidification leads to a macroscopic redistribution of constituents known as macrosegregation; freckles or channels is a typical manifestation.

---

[1] Equilibrium at the interface is closely approximated for most solidification conditions. At extremely high interface velocities (approx. 1 m/s), the interface is not at equilibrium. These exceptional cases are not treated in this dissertation.

1.3 Experimental Observations

Systems where channel segregation or freckling occurs are, among others, Pb-Sn, Ni-Al, Al-Cu, Zn-Al and several austenitic stainless steels and nickel-base superalloys. Freckles are observed as long and narrow trails, aligned parallel to the direction of gravitational force during the solidification process, that are enriched in the normally segregating elements and depleted of the inversely segregating elements; i.e. their composition is shifted toward the eutectic composition. In horizontally solidified ingots of steel, the segregation defects look like short streaks, tilted with respect to the gravity direction, and are known as "A" segregates, while in base chilled castings they have a more pronounced channel shape and are termed "freckles". The name freckles was suggested by the spotted appearance of these trails in macroetched transverse sections, due to the presence of excess solute, higher porosity and small randomly oriented grains.

Because the opacity of metals prevents direct visualization of the nucleation and growth of channels during solidification, many researchers have resorted to transparent model systems. Transparent systems which have low entropies of melting and thus exhibit metallic solidification behavior (i.e.,

with cellular or dendritic growth structure). These include various organic compounds (e.g., camphor, carbon tetrabromide, succinonitrile) and aqueous solutions of some salts (e.g., NH_4Cl). Although all these systems provide acceptable analogs for qualitative observations of transport behavior in binary mixtures, aqueous solutions of ammonium chloride have been used in most experimental studies because a more complete database of thermophysical properties is available, thus allowing quantitative comparisons with analytical models. Reported observations of channel segregation using NH_4Cl-H_2O solutions include McDonald and Hunt[3,4], Copley et al.[5], Sample and Hellawell[6,7], and Chen and Chen[8]. In each of these studies, it has been seen clearly that freckles are a direct consequence of upward flowing liquid jets that emanate from within the mushy zone, produced by a density inversion near the dendritic front. The density inversion occurs whenever the vertical liquid density gradient with concentration, $\partial\rho/\partial C_L$ is positive and exceeds the negative variation with temperature, $\partial\rho/\partial T$. In the case of a binary mixture this requires that the solute be less dense than the solvent if it segregates normally, or more dense if it segregates inversely. Because a density inversion also occurs in metallic systems where freckles are observed, it was proposed by Copley et al.[5] and further supported in later works,[4,7,9,10] that buoyancy driven convection is responsible for channel segregation.

The validity of the use of ammonium chloride-water solutions and other water-based systems to simulate the solidification of castings, however, has been questioned.[11] Although the influence of buoyancy effects in segregation seems to be evident, the large differences in thermal conductivities, solid-liquid densities and, in particular, the fraction of liquid in the dendritic structure can lead to a convection pattern that is very different from that observed in the water mixtures. This fact has been visualized in experiments with Pb-Sn, using radioactive tracer techniques[12,13], and also reported in analytical models of thermosolutal convection in dendritic alloys.[14-16] The very low, non-uniform and anisotropic permeability of a metallic dendritic assembly must undoubtedly affect the flow path, and hence the sites where channels can nucleate and grow. This fact will be illustrated in this work through numerical examples.

In laboratory experiments with metallic systems, Pb-Sn alloys have been used extensively because of the ease of handling resulting from their low melting temperatures and also because their physical properties are available. Reported experiments with lead-tin alloys include Kou et al.[17,18], Ridder et al.[19,20], Sample and Hellawell[7], Laxmanan et al.[2], Sarazin and Hellawell[21], and Tewari and Shah[22]. Again it is found that convection is the major cause of essentially all forms of observed macrosegregation. The occurrence of

convection can be deduced by the deviation of the measured temperature and solute profiles from what would be expected in the case of pure diffusion. Measurements of macrosegregation are usually done by quenching the ingot at different stages of solidification and analyzing the solidified microstructure. Freckles have been found both at the outer surface of the casting (Tewari and Shah[22]) and in the interior (Sarazin and Hellawell[21]). Other metallic systems have also been investigated including Ni-Mo (Ridder et al.[19]), Al-Cu (Flemings and Nereo[23]) and Ni-base superalloys (Giamei and Kear[9]). In Ni-base superalloys, freckles are found only at the outer surface of the casting (Giamei and Kear[9]). Each study indicates that high solidification rates and low permeability in the mushy zone tend to diminish interdendritic flow and thus lead to less severe macrosegregation. It is also found that convection in the melt can hardly penetrate into the dendritic array (Verhoeven[24]), an observation also supported by a recent numerical analysis (Heinrich et al.[15]). Freckles develop only when the rejected solute is less dense than the solvent and are therefore a result of density inversion, confirming the findings of Copley et al.[5] with ammonium chloride - water mixtures. Investigations of the influence of rotation at low speeds on macrosegregation have also been reported (Sample and Hellawell[7]). Results indicate that mold rotation about an axis inclined to the vertical, throughout the time of solidification, can effectively prevent the formation and propagation of channels.

1.4 Numerical Modeling

The prediction of transport processes during dendritic solidification (i.e. with a mushy zone) of binary alloys requires the solution of the equations of conservation of mass, momentum, energy and solute content, in a domain that includes an all-liquid region, a solid plus liquid region or mushy zone and an all-solid region. The dendritic structure in the mushy zone is usually modeled as a porous medium, with the permeability depending on the dendrite arm spacings and the fraction of solid.

In multiple region models, the conservation equations are solved independently for each region and then coupled through appropriate boundary conditions at the interfaces solid/mush and mush/liquid. The difficulty with these models centers around tracking the interfaces, which are generally unknown functions of space and time. An assumption on the shape of the mushy zone or on the solidification rate is usually invoked to avoid this problem. Examples of this type of formulation include Flemings and Nereo [23], Mehrabian et al. [10], Fuji et al. [49], Ridder et al. [20] and Maples and Poirier[50].

In single region or continuum models, a single set of equations is developed through the application of mixture theory. The equations are valid in the whole domain, irrespective of the particular region under consideration, and no internal boundary conditions are necessary. Examples of such models include Bennon and Incropera[27], Beckerman and Viskanta[28], and Heinrich et al.[15].

In addition to solving the conservation equations, both models assume local equilibrium between the liquid and solid phases in the mushy zone, and make use of the corresponding equilibrium phase diagram.

In many of the early works (e.g., Flemings and Nereo[23] and Mehrabian et al.[10]), the temperature or the concentration distribution or the solidification rates were assumed to be known (from experiments). This assumption was first relaxed by Fuji et al.[49], who coupled the energy and momentum equations, keeping Darcy's law as the momentum equation in their model. Due to the presence of preferential flow channels in the mushy zone, however, Darcy's law is not suitable to predict channel formation, according to Kaempffer and Weinberg[51], or to describe the fluid flow in the vicinity of the dendrite tips, where the fraction of liquid is close to one. Extensions to the momentum equation were added in later works, including Bennon and

Incropera[27], Beckerman and Viskanta[28] and Ganesan and Poirier[34], although there is no general agreement on the form of the equation.

Heinrich et al.[15], using a finite element model, performed nonlinear calculations to model thermosolutal convection in vertical solidification of Pb-Sn alloys. Their results compared well with a previous stability analysis by the same authors (Nandapurkar et al.[14]). However, this model could not predict channels or freckles because it assumed a pre-existing mushy zone whose shape did not change with time.

Models that allow the free growth of the mushy zone from an initially all-liquid alloy, have recently been formulated. Bennon and Incropera[25-28] and Beckermann and Viskanta[29,30] simulated horizontal solidification of aqueous solutions of ammonium chloride. The calculations showed strong double-diffusive effects and the development of irregularities in the growth front, including pockets of segregated liquid within the mushy zone that appear to be similar to the "A" segregates that form in steel ingots and large steel castings. Their results agree in qualitative features with experiments, but fail to achieve close quantitative agreement. A major assumption in these models is the use of the lever rule to obtain the concentration of the solid from the equilibrium phase diagram, neglecting the microsegregation occurred during solidification. This is of particular importance in alloys that undergo a large

change of composition during solidification, as lead-rich Pb-Sn alloys, resulting in a highly microsegregated solid.

The prediction of freckles or "A" segregates in Pb-Sn or other metallic alloys has not yet been reported.

CHAPTER 2 - MATHEMATICAL MODEL

2.1 Introduction

The model that has been implemented is two dimensional and is an extension of previous works [14-16]. The physical situation consists of an initially liquid binary alloy contained in a rectangular mold which is cooled at the base with a specified rate. The alloy begins to solidify forming a dendritic zone comprising solid and liquid that advances upward, and the solidification proceeds until all the initial melt is completely solidified.

The dendritic zone (deemed the mushy zone by metal casters) is represented mathematically by an anisotropic porous medium of variable porosity, and it is free to develop according to thermodynamic constraints, i.e. it has no predetermined shape or size. The equations of conservation of mass, momentum, energy and solute content are solved in a two dimensional domain (Fig. 1) under the following assumptions:

(i)   The flow is laminar.
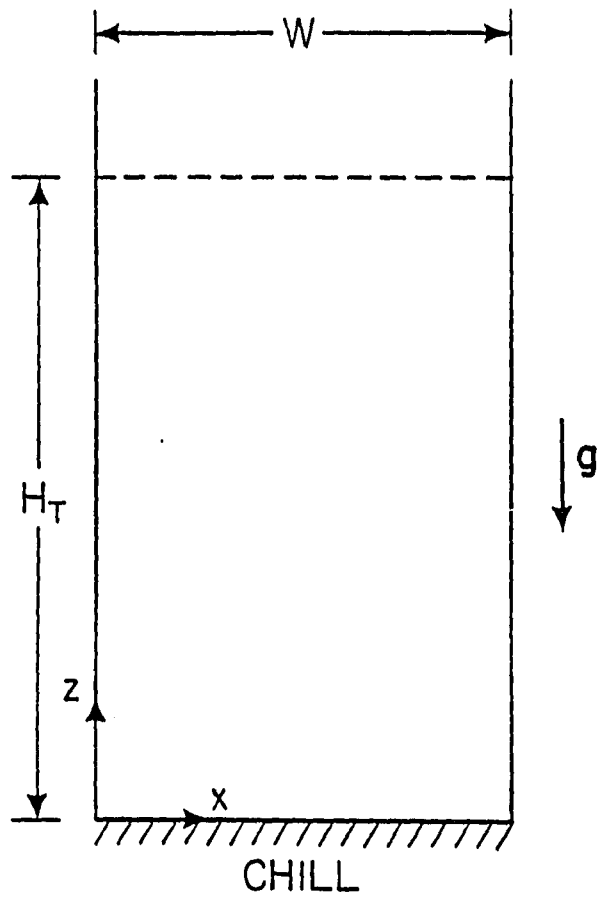
Fig. 1: Domain and coordinate system for vertical solidification.

(ii)	Only solid and liquid phases are present, i.e. no pores form.
(iii)	The solid and liquid phases have equal densities.
(iv)	The density is constant except in the buoyancy term of the momentum equation.
(v)	There is negligible diffusion of solute within the solid.
(vi)	The solid does not convect.
(vii)	The thermal properties are constant and equal in both the liquid and solid phases.

2.2 Governing Equations

2.2.1 Conservation of Mass and Momentum

Ganesan and Poirier[34] give derivations for the conservation of mass and conservation of momentum for flow in a mushy zone of variable porosity (i.e., variable volume fraction of interdendritic liquid). Their equations are derived utilizing the technique of "local volume averaging" (Hassanizadeh and Gray[52,53], Gray[54]). In this technique, each phase is treated separately and the irregular interfaces are regarded as moving boundaries. The classical conservation equations of continuum mechanics are applied to each phase, on

the microscopic scale, and supplemented by appropriate interfacial and

boundary conditions. The solution of these equations, however, is not

practical because of the complex interfacial geometry in the mushy zone. In

order to obtain a macroscopic description of the system behavior, the equations

are first averaged (i.e., integrated) over some representative elementary volume

within the mushy zone, utilizing integral theorems. The resulting averaged

equations reflect the physics of the two-phase system, and reduce to the usual

equations for a single-phase liquid or solid when the fraction of liquid is equal

to unity or zero, respectively.

Based on the assumptions outlined in section 2.1, the mass conservation

equation is[34]

$$\frac{\partial u}{\partial x} + \frac{\partial w}{\partial z} = 0 \qquad [1]$$

where u and w are the components of the superficial velocity in the x and z

directions. The x direction is horizontal, and the z direction is antiparallel to

gravity. The superficial velocities are defined as

$$u = \phi \, u_\ell$$

$$w = \phi \, w_\ell$$

where u_i and w_i are the components of the interdendritic fluid velocity and ϕ is the volume fraction of interdendritic liquid.

From Eq. [51] in Ganesan and Poirier[34], the components of the momentum equations, under the assumptions listed in section 2.1 and neglecting the second order resistance term, reduce to

(x - momentum)

$$\phi\ \frac{\partial(u/\phi)}{\partial t} + u\ \frac{\partial(u/\phi)}{\partial x} + w\ \frac{\partial(u/\phi)}{\partial z} = -\ \frac{\phi}{\rho_0}\ \frac{\partial p}{\partial x} +$$

$$\upsilon_0 \left(\frac{\partial^2 u}{\partial x^2} + \frac{\partial^2 u}{\partial z^2} \right) - \frac{\upsilon_0 \phi}{K_x}\ u$$

[2]

(z - momentum)

$$\phi\ \frac{\partial(w/\phi)}{\partial t} + u\ \frac{\partial(w/\phi)}{\partial x} + w\ \frac{\partial(w/\phi)}{\partial z} = -\ \frac{\phi}{\rho_0}\ \frac{\partial p}{\partial z} +$$

$$\upsilon_0 \left(\frac{\partial^2 w}{\partial x^2} + \frac{\partial^2 w}{\partial z^2} \right) - \frac{\upsilon_0 \phi}{K_z}\ w - \phi\ \frac{\rho}{\rho_0}\ g$$

[3]

where t is time, p is pressure, υ_0 is the kinematic viscosity and ρ_0 is the density

at a reference state, g is the gravitational acceleration, and K_x and K_z are the

permeabilities in the x and z directions, respectively.

The density, ρ, is assumed to be a linear function of the temperature, T,

and the solute concentration of the liquid, C_l

$$\rho = \rho_0 \left[1 - \beta_T (T - T_0) - \beta_C (C_l - C_0) \right]$$ [4]

where β_T is the thermal expansion coefficient, and β_C is the solutal expansion

coefficient. For the reference state, the concentration is that of the initial melt

(C_0) and the temperature is the liquidus temperature (T_0) corresponding to C_0

on the equilibrium phase diagram.

It is known that the fluid flow in the mushy zone is strongly dependent

on the choice of the permeability in columnar dendritic structures.[35] A

formulation based on an anisotropic permeability has been chosen because of

the very aligned pattern of the primary dendrite arms in the growth direction.

Experimental and analytical data of flow perpendicular and parallel to

columnar dendrites[35,36] show that the corresponding permeabilities can differ

by as much as a factor of 2. Equations used for permeabilities are given in the

Appendix, with $K_x = K_x(\phi, d_1)$ and $K_z = K_z(\phi, d_1)$, where d_1 is the primary dendrite arm spacing.

Equations [2] and [3] are similar to the component equations used by Beckermann and Viskanta[29] and later by Heinrich et al.[15] They differ in the terms containing the partial derivatives of ϕ^{-1}. These terms are not important deep inside the mushy zone, where ϕ is less than about 0.6 and the Darcy, pressure, and body force terms dominate. On the other hand, the added terms containing derivatives in ϕ^{-1} have been shown to affect the number of convection cells in the upper part of the mushy zone, as well as the kinetic energy of the convection in the all-liquid and mushy zones.[37]

2.2.2 Conservation of Energy and Solute Content

The equations of conservation of energy and solute content derived by Poirier et al.[38] are used in this study.

The energy equation, as given in their Eq. [10] is

$$\bar{\rho} \frac{\partial \bar{h}_s}{\partial t} + g_L \rho_L \frac{\partial L}{\partial t} - L \frac{\partial}{\partial t}(g_s \rho_s) = \nabla \cdot (\kappa \nabla T) - \rho_L \vec{u} \cdot (\nabla \bar{h}_s + \nabla L) \qquad [5]$$

where $\bar{\rho}$ is the density of the two phase mixture, $\bar{h}_s$ is the average intensive enthalpy of the solid, L is the latent heat defined as $L = h_L - \bar{h}_s$, h_L is the intensive enthalpy of the liquid, ρ_L and ρ_s are the densities of liquid and solid, $g_L = \phi$ is the volume fraction of liquid, $g_s = 1 - \phi$ is the volume fraction of solid, T is temperature, $\vec{u}$ is the superficial velocity vector, and κ is the effective thermal conductivity of the solid plus liquid mixture.

If, in addition to the assumptions listed in section 2.1, the latent heat L is assumed constant, and we substitute

$$\frac{\partial \bar{h}_s}{\partial t} = c_s \frac{\partial T}{\partial t} \qquad [6]$$

and

$$\nabla \bar{h}_s = c_s \nabla T \qquad [7]$$

where c_s is the specific heat of the solid, then the energy equation in the mushy zone reduces to

$$\frac{\partial T}{\partial t} + u \frac{\partial T}{\partial x} + w \frac{\partial T}{\partial z} = \alpha \left(\frac{\partial^2 T}{\partial x^2} + \frac{\partial^2 T}{\partial z^2} \right) - \frac{L}{c_s} \frac{\partial \phi}{\partial t} \qquad [8]$$

where $\alpha = \kappa / \rho c_s$ is an effective thermal diffusivity.

By stating the solute balance in a volume element containing solid plus liquid mixture, in which solute enters and leaves the element by Fickian

diffusion through the liquid and by advection of the interdendritic liquid, the equation of conservation of solute mass can be written as[38]

$$\frac{\partial \bar{C}}{\partial t} + u\,\frac{\partial C_l}{\partial x} + w\,\frac{\partial C_l}{\partial z} = D\left[\frac{\partial}{\partial x}\left(\phi\,\frac{\partial C_l}{\partial x}\right) + \frac{\partial}{\partial z}\left(\phi\,\frac{\partial C_l}{\partial z}\right)\right] \qquad [9]$$

where D is the solutal diffusivity in the liquid (assumed to be constant), and $\bar{C}$ is the local average composition of liquid and solid together; i.e.,

$$\bar{C} = \phi C_l + (1 - \phi)\bar{C}_s \qquad [10]$$

$\bar{C}_s$ is the local average composition of the solid. Here, "local average" means the average taken over a microscopic scale, which accounts for the microsegregation in the solid phase (see below).

2.2.3 Phase Diagram Constraints

In dendritic freezing processes of alloys, the composition of the interdendritic liquid at a given temperature is essentially uniform, and the local solid-liquid interface is very close to equilibrium.[39] Therefore, the composition of the interdendritic liquid must be given by the liquidus line in the phase diagram of the alloy; i.e. $C_l = C_L(T)$, where $C_L(T)$ is a function

approximating the liquidus line. A linear approximation is used in this model. In the all-liquid zone, however, C_i results from the diffusion-convection balance stated by Eq. [9]. That is,

$$C_i = \begin{cases} C_L(T) & \text{(liquidus line in the phase diagram)} & \text{if } \phi < 1 \\ \\ \bar{C} & & \text{if } \phi = 1 \end{cases} \qquad [11]$$

The model allows for microsegregation within the local solid, so the composition of a volume element of solid, $\bar{C}_s$, is not uniform. The "bar" indicates that an average value must be calculated. When a melt of composition C_0 begins to solidify, the first solid that forms has composition kC_0, where k is the equilibrium partition ratio of the alloy, defined as the ratio between the compositions of the solid and liquid phases at the solid/liquid interface. As solidification proceeds, the liquid becomes richer in solute and so does the new solid that forms. However, the solid that formed at the earlier stages of solidification kept the same composition of solute, since no diffusion in the solid has occurred. Thus, the composition of the solid in the volume element is calculated as the average of the values at the solid/liquid interface during the solidification history. Mathematically,

$$\bar{C}_s = \frac{1}{1 - \phi} \int_{\phi}^{1} kC_l \, d\phi \qquad [12]$$

where k is the equilibrium partition ratio.

Using Eq. [12], Eq. [10] can be rewritten as

$$\bar{C} = \phi C_l + I \qquad [13]$$

where

$$I = \int_{\phi}^{1} kC_l d\phi \qquad [14]$$

The Pb-10 wt pct Sn alloy, for which the stated assumptions are approximate, is used for most of the numerical experiments in this study. The Pb-Sn equilibrium phase diagram is shown in Fig. 2.

2.3 Numerical Scheme

The conservation equations are solved by the finite element method, using a penalty function, Petrov-Galerkin formulation. The details of the implementation are addressed by Heinrich.[44,45]
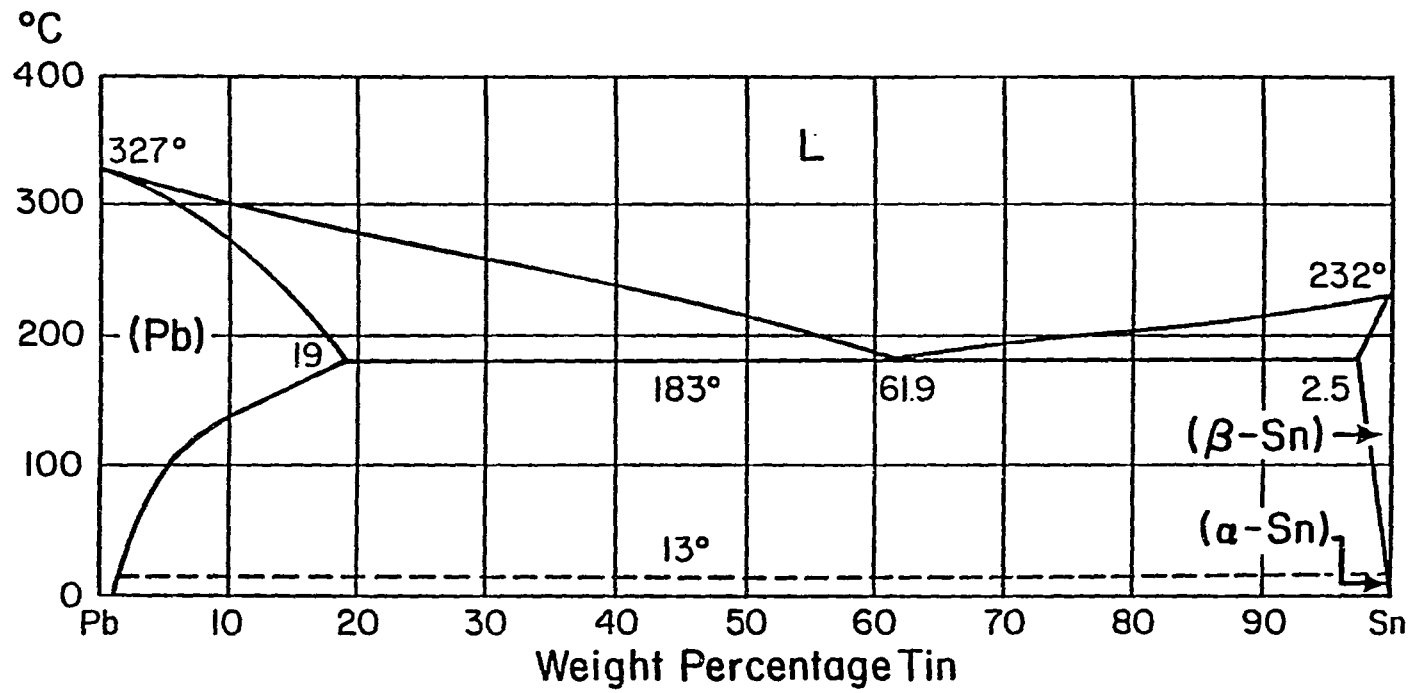
Fig. 2: Pb-Sn phase diagram.

It is assumed that all variables are known at time $t = t_n$. To advance to time $t_{n+1} = t_n + \Delta t$, the governing equations are solved iteratively, in the sequence of steps specified below. In each step, a variable is computed using the latest available values of all the other variables on which it depends.

1. $n = 0$; u_0, w_0, T_0, etc. are known (initial conditions).

2. Time step $n + 1$; $t_{n+1} = t_n + \Delta t$

    $i = 0$; $u_{n+1}^{i=0} = u_n$, $w_{n+1}^{i=0} = w_n$, $T_{n+1}^{i=0} = T_n$, etc.

3. Iteration $i + 1$

4. Compute u_{n+1}^{i+1} and w_{n+1}^{i+1} from Eqs. [1]-[4].

5. Compute T_{n+1}^{i+1} from Eq. [8].

6. Set

$$C_{t_{n+1}}^{i+1} = \begin{cases} C_L(T_{n+1}^{i+1}) & \text{if } C_{t_{n+1}}^{i} \leq C_L(T_{n+1}^{i+1}) \\ \\ \bar{C}_{n+1}^{i} & \text{if } C_{t_{n+1}}^{i} > C_L(T_{n+1}^{i+1}) \end{cases} \qquad [15]$$

where $C_L(T_{n+1}^{i+1})$ is obtained from the liquidus line in the phase diagram.

7. Calculate ϕ_{n+1}^{i+1} from Eq. [10] in the form

$$\phi_{n+1}^{i+1} = \frac{(\bar{C}_{n+1}^{i} - I_{n+1}^{i})}{C_{t_{n+1}}^{i+1}} \qquad [16]$$

8. For nodes in which $0 < \phi_{n+1}^{i+1} < 1$, compute I_{n+1}^{i+1} from Eq. [14].

9. Compute $\bar{C}_{n+1}^{i+1}$ from Eq. [9].

10. Recalculate ϕ_{n+1}^{i+1} from Eq. [16].

11. If $\| \phi_{n+1}^{i+1} - \phi_{n+1}^{i} \| < \varepsilon$ (tolerance) then

$$u_{n+1} = u_{n+1}^{i+1}, \; w_{n+1} = w_{n+1}^{i+1}, \; \text{etc}$$

$$n = n + 1$$

go to 2.

else

$$i = i + 1$$

go to 3.

end if

During each time step, Steps 3-11 are solved iteratively until convergence in ϕ is achieved, before advancing to the next time step. In this work, Step 1 was solved only once per time step, because the velocities were found to vary very little (less than 1%) during iterations. At the end of each time step, the concentration of the solid, $\bar{C}_s$, is calculated from Eq. [12].

The integral I in Eq. [14] is computed incrementally; i.e. at each time step only the increment corresponding to the change in ϕ is added to the value of I at the previous time step. The increment can be positive or negative, depending whether the volume element has undergone solidification or

remelting, respectively. If the increment is positive, it is computed from Eq. [14]. If it is negative (remelting), the value of I is calculated from the solidification history. The solidification history consists of saved values of ϕ and I at previous time steps. These values are not saved at every time step, which would be very memory expensive, but rather at selected time steps. In the present model, the history is saved at 100 equally spaced values of ϕ, i.e. every increment of 0.01 in fraction of liquid. Linear interpolation is used for other values of ϕ.

The time step size, Δt, is selected so that convergence is achieved in 2 or 3 iterations within the time step. As explained in section 2.5, the energy equation Eq. [8] must be rewritten in the implicit form of Eq. [21] for the algorithm to converge. Variations of the algorithm described above can be implemented in order to save computational time. For example, if the time step size is not too big (convergence is reached in 2 or 3 iterations), it is not necessary to recompute the matrix of Eq. [21] in every iteration; rather it is computed only once per time step.

2.4 Remelting

It is possible that remelting occurs in some regions of the mushy zone during solidification. Remelting is an important mechanism in the formation of channels and requires careful consideration.

Consider a differential volume element within the mushy zone that has a fraction liquid ϕ_1 in Fig. 3. Its temperature and liquid concentration are given by the point (T_1, C_{l1}) in the liquidus line. Remelting occurs in this element when $\partial \phi / \partial t > 0$, without necessarily achieving a fraction liquid of one. In order for this to happen, either the temperature or the concentration of the element must increase (assuming $k < 1$). Heat is extracted during solidification, so temperature is not expected to increase, not even by advective flow of hotter liquid into the element because of the high thermal diffusivity of metals. Instead, the concentration increases by the advection of solute-rich fluid into the volume, so the volume element adjusts itself to the point (T_2, C_{l2}) on the liquidus line with $C_{l2} > C_{l1}$ and $T_2 < T_1$.

If we follow the evolution of the concentration of the solid phase in the volume element during remelting, we have the situation shown in Fig. 3, where $g_s = 1 - \phi$ is the volume fraction of solid and $C_s^* = kC_l$ is the concentration of the solid at the solid-liquid interface. From point 0 to 1 normal solidification has taken place; from point 1 to 2 the volume element partially remelts, increasing its fraction liquid from ϕ_1 to ϕ_2. Note that the
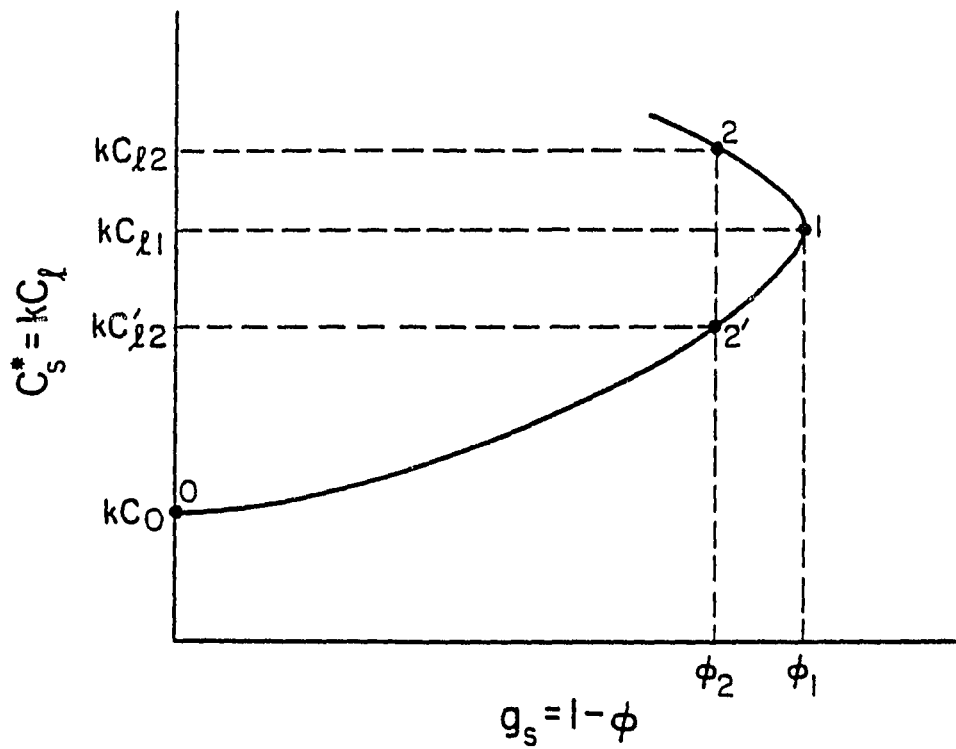
Fig. 3: Microsegregation during solidification and remelting.

condition of equilibrium at the interface requires that the composition of the solid here be kC_{l2} and not kC'_{l2}, as it was during the solidification part of the curve. However, the amount of solute contributed to the liquid by remelting is given by the enclosed area $\phi_2\phi_1 12'$ and not by $\phi_2\phi_1 12$, while the new average composition of the solid in the volume element is the same as it was at point $2'$ of the solidification history. During remelting, therefore, the average composition of the solid cannot be computed from Eq. [12], but it must be taken from the solidification history. Because we cannot predict where or when remelting occurs, the microsegregation curve has to be saved for every node in the finite element mesh.

2.5 Modified Energy Equation

The latent heat term in Eq. [8] must be treated implicitly in order for the numerical algorithm to be stable. We proceed to eliminate ϕ from Eq. [8] by using Eqs. [9]-[12]. Equations [10] and [12] can be combined in:

$$\overline{C} = \phi C_l + I \qquad [17]$$

where $I = \int_\phi^1 kC_l \, d\phi$ is the amount of solute in the solid phase of the volume

element (area under the microsegregation curve in Fig. 3). From Eq. [17], we

write

$$\frac{\partial \overline{C}}{\partial t} = \phi \, \frac{\partial C_l}{\partial t} + C_l \, \frac{\partial \phi}{\partial t} + \frac{\partial I}{\partial t} \qquad [18]$$

Note that in Eq. [18], we cannot say that

$$\frac{\partial}{\partial t}\left(\int_\phi^1 kC_l \, d\phi\right) = -kC_l\frac{\partial \phi}{\partial t} \qquad [19]$$

as in Flemings and Nereo[39], because this is not valid during remelting, as

explained in §2.4

Considering the liquidus as a straight line with slope m ($m < 0$), the

temperature is related to C_l in the mushy zone by

$$T = T_M + mC_l \qquad [20]$$

where T_M is the melting point of the solvent. Equations [9], [18] and [20] can

be substituted into Eq. [8], resulting in:

$$\left(1 - \tilde{L}\frac{\phi}{C_l}\right)\frac{\partial T}{\partial t} + \left(1 - \frac{\tilde{L}}{C_l}\right)\left(u\frac{\partial T}{\partial x} + w\frac{\partial T}{\partial z}\right) - \alpha\left(\frac{\partial^2 T}{\partial x^2} + \frac{\partial^2 T}{\partial z^2}\right)$$
$$- \frac{D\tilde{L}}{C_l}\left[\frac{\partial}{\partial x}\left(\phi\frac{\partial T}{\partial x}\right) + \frac{\partial}{\partial z}\left(\phi\frac{\partial T}{\partial z}\right)\right] + \frac{m\tilde{L}}{C_l}\frac{\partial I}{\partial t} \qquad [21]$$

where $\tilde{L} = L/mc_s$.

Equation [21] replaces Eq. [8] in the numerical algorithm. Note that, because of Eq. [20], Eq. [21] is not uniformly valid throughout the domain; i.e. if we set $\phi = 1$ in Eq. [21] we do not obtain the energy equation in the all-liquid zone. Therefore, the terms containing the parameter $\tilde{L}$ must be computed only for the elements in the mushy zone, where $C_l = C_L(T)$.

2.6 Solidification at Eutectic Temperature

While pure metals solidify at discrete temperatures, binary alloys exhibit melting and freezing over a range of temperatures. During solidification, for a given temperature, the composition of the interdendritic liquid and the composition of the solid at the local solid/liquid interface, are given by the liquidus and solidus lines of the equilibrium phase diagram. In this regime, the temperature changes are governed by the energy equation [8]. According

to the numerical scheme outlined in section 2.3, the solidification algorithm
proceeds as follows:

1. A decrease in the temperature of a volume element in the mushy
   zone automatically results in an increase in the concentration of
   the liquid, given by Eq. [15].

2. An increase in the concentration of the liquid in turn produces a
   decrease in the fraction of liquid, according to Eq. [16].

In other words, the temperature is the variable that drives the solidification.
However, when a volume element reaches the eutectic temperature, the
remaining liquid in the element, according to thermodynamic equilibrium,
solidifies at constant temperature. Consequently, the solidification algorithm
does not work at this point.

In formulations with an enthalpy-based energy equation (e.g. Bennon
and Incropera[25]), this problem is avoided by computing the fraction of liquid
at eutectic in terms of the mixture enthalpy, since the enthalpy equation is still
valid at the eutectic temperature. The energy equation in terms of the mixture
enthalpy can be written as (Poirier et al.[38])

$$\frac{\partial h}{\partial t} = \frac{1}{\rho}\nabla\cdot(\kappa\nabla T) - \vec{u}\cdot\nabla h_L \qquad [22]$$

where h is the enthalpy of a volume element containing solid plus liquid

mixture. If we substitute

$$h = \bar{h}_s + \phi L \qquad\qquad [23]$$

we obtain Eq. [5].

From Eq. [22], it is observed that when a point solidifies at constant

temperature, its enthalpy continues changing due to local temperature

gradients or boundary conditions. Then, the fraction of liquid ϕ can be

computed from Eq. [23], with h the variable that drives the solidification.

Although enthalpy formulations are undoubtfully more comprehensive

than temperature approaches, they require an h to T transformation, since

temperature is ultimately the measurable quantity and in terms of which

boundary conditions and physical properties are specified. Unfortunately,

direct algebraic h-T transformations are possible only for simple

thermophysical property descriptions, such as constant specific heats and

complete diffusion in the solid. In particular, the last assumption; i.e. complete

diffusion in the solid, yields a direct relation of ϕ as a function of T, which,

after substituting in Eq. [23], and assuming linear dependence of the phase

enthalpies with temperature, results in an algebraic equation for T as a

function of the mixture enthalpy.[25] For more general cases, with variable

properties or when microsegregation in the solid is involved, iterative solutions

of nonlinear relations are required. These iterative procedures present stability problems and require computationally costly implicit schemes.

In order to retain the simplicity of the temperature formulation, an alternative approach is followed to solve the problem of solidification at constant temperature. When a region in the computational domain is at the eutectic temperature, the energy equation [8] is used, instead, as an equation for the fraction of liquid, by setting the term with the time derivative of T equal to zero. From Eq. [8] we obtain

$$\frac{\partial \phi}{\partial t} = \alpha \frac{c_s}{L} \nabla^2 T - \frac{c_s}{L} \vec{u} \cdot \nabla T \qquad [24]$$

Note that Eq. [24] is essentially Eq. [5] with constant heat of fusion and constant density, and where the time derivative of the phase enthalpies is now equal to zero. Equation [24] is solved only for those regions that are solidifying at constant temperature; the complete energy equation, Eq. [8], is solved elsewhere. Except in the case of a fraction of liquid close to one at eutectic, due to the low permeability, the velocities in the regions that have reached the eutectic temperature, are very small, and the convective term in Eq. [24] can be neglected. It is also seen from Eq. [24] that the time a region will stay at eutectic temperature before solidifying completely is proportional to L/κ.

It is important to note that, physically, the eutectic isotherm advances smoothly through the domain; that is, a material point does not stay at eutectic temperature for a finite period of time. The velocity of the eutectic isotherm depends on how fast the latent heat is transported away from the solid/liquid interface. The present model, however, does not deal with internal solid/liquid interfaces but with volume averaged quantities in a porous medium. Hence, numerically, a volume element or mesh point is solidified at constant temperature until it is completely solid. After that, its temperature continues to be calculated with Eq. [8]. In other words, the movement of the eutectic isotherm is followed in a step-wise form. Verification of this method of treating the solidification of the eutectic is given in § 3.1.3.

2.7 Nondimensionalization

Finally, the governing equations are nondimensionalized before solving them numerically. By making use of a reference length, H, chosen later, and a reference thermal gradient, G, the reference velocity is defined as

$$U = \left(g\, \beta_T\, G\, H^2 \right)^{1/2} \qquad [25]$$

Accordingly, the nondimensional velocity components and spatial coordinates become:

$$u = u'/U \quad \text{and} \quad w = w'/U$$

$$x = x'/H \quad \text{and} \quad z = z'/H$$

where the prime denotes a dimensional quantity. Thus, we write the continuity equation as

(continuity)

$$\frac{\partial u}{\partial x} + \frac{\partial w}{\partial z} = 0 \qquad [26]$$

where it is understood that the variables have been nondimensionalized.

For the components of the remaining conservation equations, the following nondimensional parameters are used:

1. $Ra_T = \dfrac{g\,\beta_T\,G\,H^4}{v_0\,\alpha}$,   Thermal Rayleigh number.

2. $Ra_s = \dfrac{g\,\beta_c\,C_0\,H^3}{v_0\,D}$,   Solutal Rayleigh number.

3. $Pr = \dfrac{v_0}{\alpha}$,   Prandtl number.

4. $Sc = \dfrac{v_0}{D}$ Schmidt number.

5. $\quad Da_x = \dfrac{K_x}{H^2}$ and $Da_z = \dfrac{K_z}{H^2},$ Darcy numbers in x and z directions, respectively.

In addition, we define a reference time

$$\tau = \frac{H^2}{v_0},$$

and a reference pressure,

$$P = \frac{\rho_0 H^2}{\tau^2},$$

The temperature and solute concentration are nondimensionalized according to

$$T = \frac{T' - T_0}{GH}, \quad C_\ell = \frac{C_\ell'}{C_0}, \quad \text{and} \quad \bar{C} = \frac{\bar{C}'}{C_0}, \quad \text{where } T_0 \text{ is the liquidus}$$

temperature of the initial melt with concentration C_0.

Finally the nondimensional pressure is defined as

$$p = p^*/P$$

where p^* is a dimensional pressure that satisfies

$$\nabla p^* = \nabla p' + \rho_0 g.$$

The remaining conservation equations become:

(x-momentum)

$$\left(\frac{Pr}{Ra_T}\right)^{1/2}\left\{\phi\,\frac{\partial(u/\phi)}{\partial t} - \left(\frac{\partial^2 u}{\partial x^2} + \frac{\partial^2 u}{\partial z^2}\right) + \frac{\phi}{Da_x}\,u\right\} = -\phi\left(\frac{Pr}{Ra_T}\right)\frac{\partial p}{\partial x}$$

$$-\left(u\,\frac{\partial(u/\phi)}{\partial x} + w\,\frac{\partial(u/\phi)}{\partial z}\right)$$

[27]

(z-momentum)

$$\left(\frac{Pr}{Ra_T}\right)^{1/2}\left\{\phi\,\frac{\partial(w/\phi)}{\partial t} - \left(\frac{\partial^2 w}{\partial x^2} + \frac{\partial^2 w}{\partial z^2}\right) + \frac{\phi}{Da_z}\,w\right\} = -\phi\left(\frac{Pr}{Ra_T}\right)\frac{\partial p}{\partial z}$$

$$-\left(u\,\frac{\partial(w/\phi)}{\partial x} + w\,\frac{\partial(w/\phi)}{\partial z}\right) + \phi\left[T + \frac{Ra_s\,Pr}{Ra_T\,Sc}\,(C_i - 1)\right]$$

[28]

(energy)

$$\left(1 - \hat{L}\,\frac{\phi}{C_i}\right)\frac{\partial T}{\partial t} - \frac{1}{Pr}\left(\frac{\partial^2 T}{\partial x^2} + \frac{\partial^2 T}{\partial z^2}\right) + \frac{\hat{L}}{Sc}\,\frac{1}{C_i}\left[\frac{\partial}{\partial x}\left(\phi\,\frac{\partial T}{\partial x}\right) + \frac{\partial}{\partial z}\left(\phi\,\frac{\partial T}{\partial z}\right)\right]$$

[29]

$$= -\left(\frac{Ra_T}{Pr}\right)^{1/2}\left(1 - \frac{\hat{L}}{C_i}\right)\left(u\,\frac{\partial T}{\partial x} + w\,\frac{\partial T}{\partial z}\right) + \bar{L}\,\frac{\partial I}{\partial t}$$

(solute concentration)

$$\frac{\partial \bar{C}}{\partial t} = \frac{1}{Sc} \left[\frac{\partial}{\partial x} \left(\phi \; \frac{\partial C_\iota}{\partial x} \right) + \frac{\partial}{\partial z} \left(\phi \; \frac{\partial C_\iota}{\partial z} \right) \right]$$
$$- \left(\frac{Ra_T}{Pr} \right)^{1/2} \left(u \; \frac{\partial C_\iota}{\partial x} + w \; \frac{\partial C_\iota}{\partial z} \right)$$

[30]

where

$$\hat{L} = \frac{L}{m \, c_s \, C_0} \qquad \text{and} \qquad \bar{L} = \frac{L}{c_s \, G \, H} \, .$$

CHAPTER 3 - NUMERICAL RESULTS

3.1 Code Verification

The program was first numerically tested solving simple problems for which an exact solution is available or applying it to cases already published in the literature.

Most of the calculations were done for a Pb-10wt pct Sn alloy. The lead-tin system has been used in many experiments of solidification, and there is a good availability of data on physical properties. The corresponding equilibrium phase diagram is shown in Fig. 2, and the thermodynamic and transport properties used in the calculations are given in Table I.

3.1.1 1-D Case with Constant Temperature Gradient

The first test corresponds to a case with no convection, constant temperature gradient, and constant solidification rate. The solution is given by the local solute redistribution equation (Eq. (3-20) in Flemings[39])

Table I

Thermodynamic and Transport Properties used for Calculations
in Pb-10 wt pct Sn

Property	Source
Reference concentration (C_0), 10 wt pct Sn	—
Reference temperature (T_0), 577 K	[40]
Equilibrium partition ratio (k), 0.31	[40]
Melting point of lead (T_M), 600 K	[40]
Slope of liquidus (m), -2.33 K·(wt pct)$^{-1}$	[40]
Density $[\rho_0 = \rho(C_0,T_0)]$, 1.01 × 10^4 kg·m^{-3}	[41]
Thermal expansion coefficient (β_T), 1.2 × 10^{-4} K^{-1}	[41]
Solutal expansion coeff. (β_C), 5.15 × 10^{-3} (wt pct)$^{-1}$	[41]
Kinematic viscosity (ν_0), 2.47 × 10^{-7} m^2·s^{-1}	[21]
Latent heat (L); kJ·kg^{-1}:	
At (C_0,T_0), 26	[43]
At (C_E,T_E), 56	[43]
Used in calculation, 37.6	
Heat capacity (c_s); kJ·kg^{-1}·K^{-1}:	
Liquid at (C_0,T_0), 0.161	[43]
Solid at (C_E,T_E), 0.173	[43]
Used in calculation, 0.167	
Thermal conductivity (κ); kW·m^{-1}·K^{-1}:	
Liquid at C_0,T_0, 0.0167	[38]
Mixture at (C_E,T_E), 0.0198	[38]
Used in calculation, 0.0182	
Thermal diffusivity $(\alpha = \kappa/\rho_0 c_s)$, 1.1 × 10^{-5} m^2·s^{-1}	[38,41]
Solutal diffusivity (D), 3 × 10^{-9} m^2·s^{-1}	[21]

$$C_i = C_0\left[\frac{a}{k-1} + \left(1 - \frac{ak}{k-1}\right)\phi^{k-1}\right]$$

[31]

where $a = DG/mVC_0$ and V is the (constant) solidification rate. Figure 4 shows calculated results after 10 min. for a case in which $G = 1$ K/mm and $V = 0.167$ mm/s. The container length is $H_T = 120$ mm and the temperature at the bottom wall was initially $T_0 = 577$ K (304 C), the freezing point of the alloy. In order to impose a constant temperature gradient at all times, the bottom and top boundaries are cooled at a rate equal to GV and a linear profile is imposed between these two points. The results show that the concentration of the liquid in the mushy zone is also linear, because we assume the liquidus to be a straight line. The calculated fraction liquid profile follows the exact solution given by Eq. [31].

3.1.2 1-D Case with Temperature Computed from the Energy Equation

A more interesting one dimensional example is presented in Fig. 5. Again, no convection is allowed, but now the temperature profile is calculated with the energy equation rather than being imposed. The alloy is initially at 593 K (320 C) in a 10 mm long container. A heat transfer coefficient h = 5.68×10^3 W·m⁻²·K⁻¹ is imposed at z = 0 and zero heat flux is prescribed at the
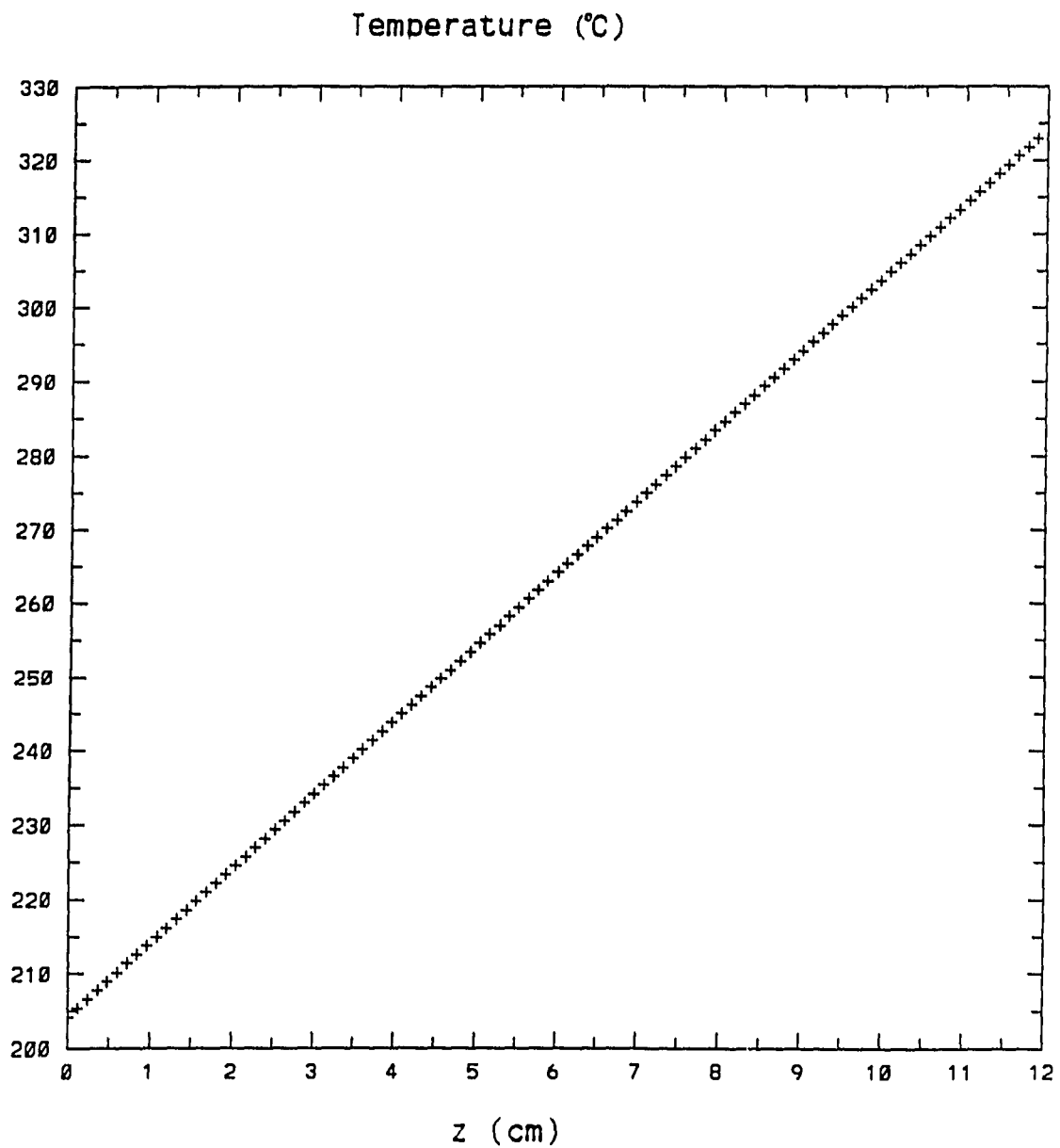
Temperature (°C)

Fig. 4: Solidification with no convection, constant temperature gradient G=1K/mm and constant growth rate V=0.167mm/s. Time = 10 min.
(a) temperature (°C)

Conc. of liquid (wt pct Sn)
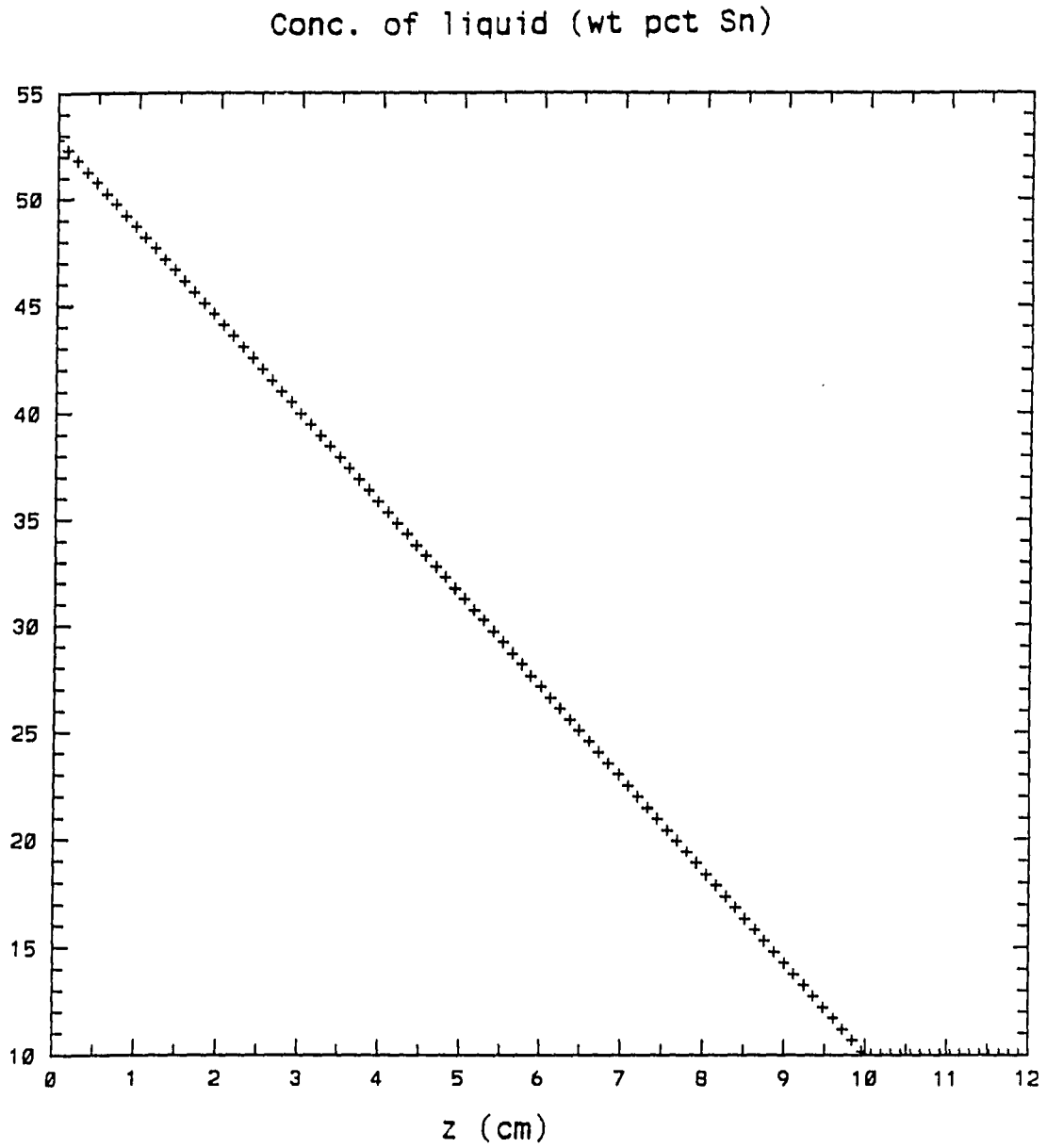
Fig. 4: (continued). (b) concentration in liquid (wt pct Sn x 10^{-1})
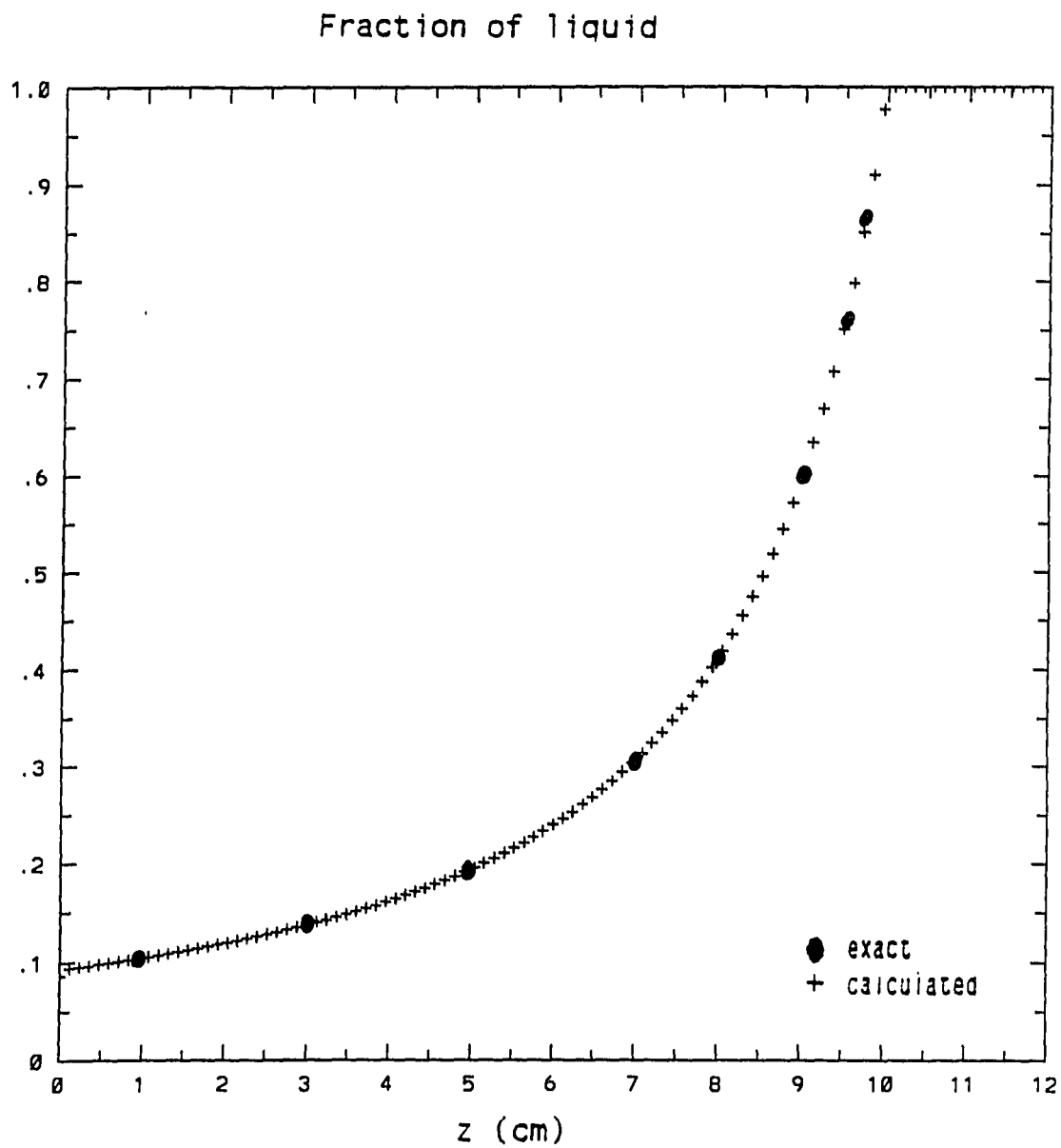
Fig. 4: (continued). (c) fraction of liquid.
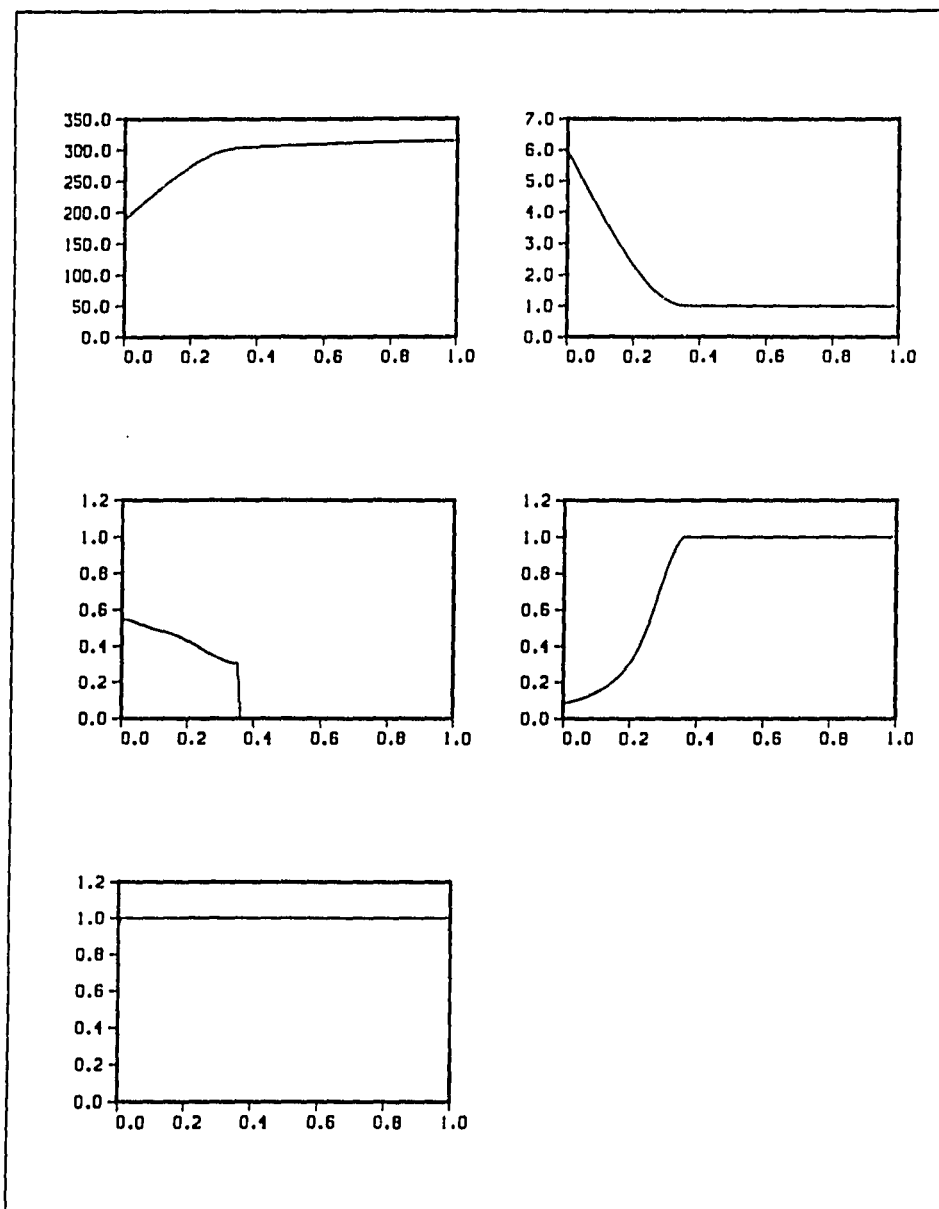
Fig. 5: 1-D solidification with temperature computed from the energy equation. From left to right and top to bottom: Temperature (°C), concentration in the liquid, conc. in the solid, fraction of liquid, and conc. of the mixture. Concentrations are in wt pct Sn x 10^{-1}. (a) Time = 2 s.
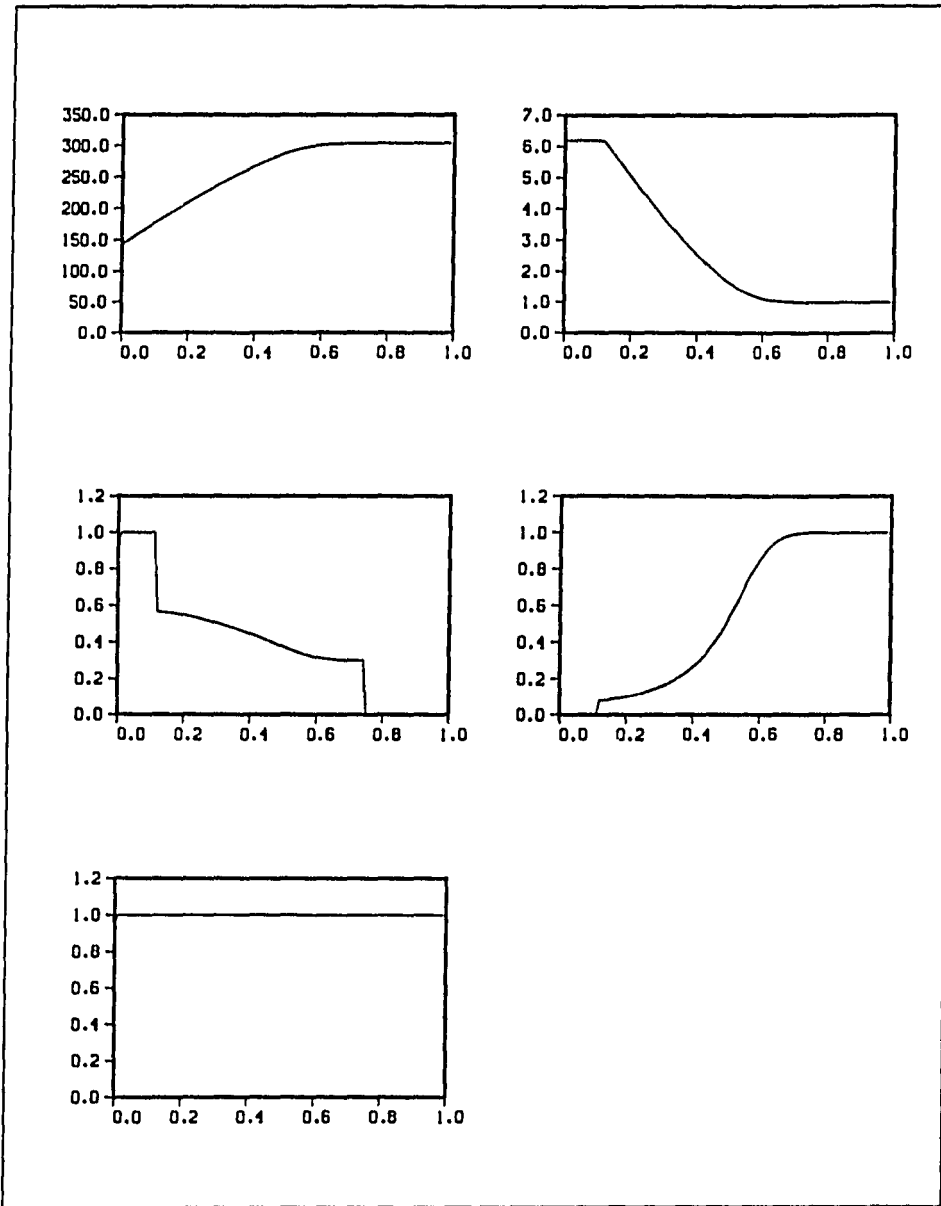
Fig. 5: (continued). (b) Time = 5 s
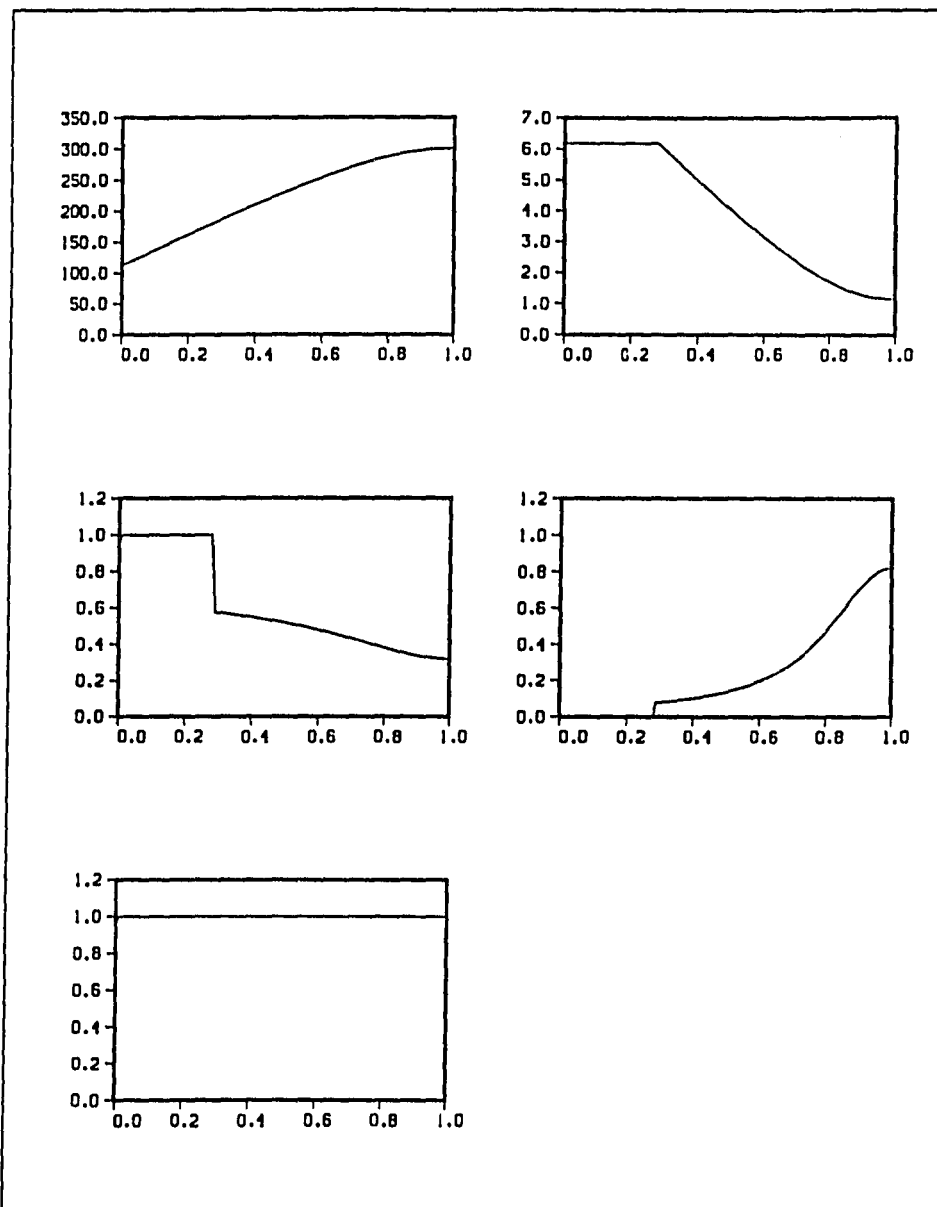
Fig. 5: (continued). (c) Time = 10 s
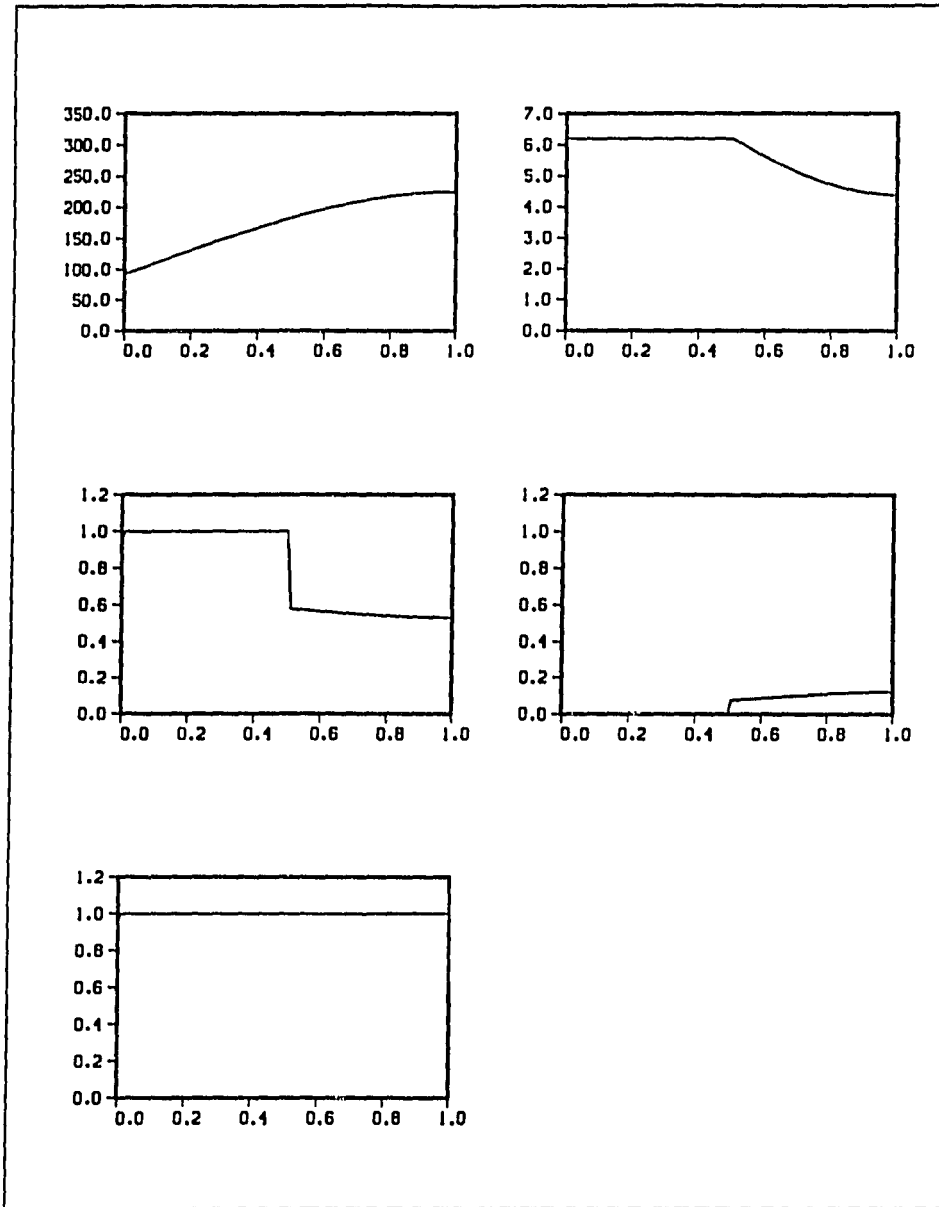
Fig. 5: (continued). (d) Time = 15 s

top and lateral walls. The ambient temperature is 293 K (20 C). After an initial transient, an almost steady solidification rate of 0.4 mm/s is reached. An approximately linear temperature profile develops in the mushy zone, except near the tips of the dendrites, with a gradient $G \cong 30$ K/mm. It can again be verified that the fraction of liquid and the concentration of the liquid in the mushy zone are related by Eq. [31] when the temperature gradient is constant. At t=15s half of the container length is completely solidified. The solidification sequence of Fig. 5 shows that although the composition of the solid is not uniform during solidification, the final composition is uniform and equal to C_0.

3.1.3 Solidification of an Alloy of Eutectic Composition

Another calculation performed to validate the code consisted in simulating the solidification of an alloy of eutectic composition. As it is well known, this alloy solidifies at a constant temperature equal to the eutectic temperature. That is, there is a solid/liquid inteHxace without a mushy zone. In fact, the code handles this discontinuity with a narrow transition region of 1 or 2 elements wide. The computational domain consisted of a 1 m high mold containing a Pb-Sn alloy of composition 61.9 wt pct tin and temperature 456K, i.e. the eutectic values. At time zero a cold temperature $T_s = 293K$ is applied at

the bottom boundary. If one dimensional conduction with no convection is considered, an analytical solution for the position of the solid/liquid interface as a function of time is given by[52]

$$z_i = 2\beta \sqrt{\alpha t} \qquad [32]$$

where β is a constant obtained from

$$\beta e^{\beta^2} erf\beta = (T_M - T_s)\frac{c_p}{H_f\sqrt{\pi}} \qquad [33]$$

In Eqs. [32] and [33], z_i is the position of the solid/liquid interface measured from the bottom boundary where T_s is prescribed, α is the thermal diffusivity, T_M is the freezing point of the alloy (in this case the eutectic temperature), c_p is the specific heat, and H_f is the latent heat per unit mass.

Table II shows good agreement between the exact solution and the calculated value of z_i. As mentioned above, the code cannot reproduce a sharp solid/liquid discontinuity, but a narrow transition region. The position of the interface is to be interpreted as the node closest to the bottom chill that has fraction of liquid equal to one.

The purpouse of this validation test is to show that, although the code is designed to model the solidification of dendritic alloys (where a mushy zone exists), it can also handle situations with a high fraction of liquid at the

Table II

Position of Interface in Solidification of Eutectic Alloy

Time (min)	z_t (calculated) (mm)	z_t (analytical) (mm)
10	75	82
20	118	117
30	141	143
40	161	165
50	180	184
60	200	202
90	249	247
120	281	286
150	319	319
180	342	350
240	410	404
300	460	452
360	490	495

eutectic point, in which case the rest of the solidification at this point proceeds at constant temperature.

3.1.4 Horizontal Solidification of a NH_4Cl-H_2O Mixture

Finally, a 2-D example with convection utilizing the full capability of the model is solved. The calculation is performed for an aqueous ammonium chloride system (NH_4Cl-70 wt pct H_2O), which exhibit dendritic growth behavior and hence is analogous to metallic alloys.

Horizontal solidification is considered in a two dimensional rectangular mold of dimensions 0.025 m wide by 0.10 m high. Initially all the mold boundaries are insulated and the cavity is filled with the ammonium chloride mixture superheated to $T = 311$ K. Solidification is induced at time zero by applying a cold temperature $T = 223$ K at the left vertical wall. The eutectic temperature of the aqueous ammonium chloride system is 257.75 K and the freezing point of the NH_4Cl-70 wt pct H_2O mixture is 305.5 K.

The eutectic composition is 80.5 wt pct H_2O. The cavity was discretized with a 40x40 finite element mesh.

This same example was solved by Bennon and Incropera[27] using an enthalpy-based continuum model and a control-volume-based difference

scheme. All the thermophysical property data, as well as the operating condition parameters, were extracted from that reference.

Figure 6 illustrates predicted macrosegregation pattern after 4 min of solidification. The bar diagram indicates values of the total concentration $\bar{C}$. Figures 7a and 7b show isoconcentrates of the liquid phase and streamlines, respectively, at time 3 min. The solidus and liquidus are also indicated by dash lines in Fig. 6.

These results compare very well with the ones shown in Fig. 2 of reference [27]. The existence of a chilled and water-rich bulk fluid region at the cavity top (Fig. 6) has been experimentally observed for the $NH_4Cl\text{-}H_2O$ system[53], and the irregular liquidus interface morphology has also been verified by numerous investigators.[3,4,53] Figure 6 illustrates the formation of two solute rich penetrations, known as "A" segregates, at the top left of the cavity. The solute-rich regions at the top come at the expense of solute depleted zones at the cavity bottom. Note that the "A" segregates form in regions of upward fluid flow, indicated by the negative (clockwise) streamlines in Fig. 7b. Note also that the convection in the bulk liquid easily penetrates into the mushy zone (region delimited by the solidus and liquidus lines), because of the high permeability of the dendritic structure of the $NH_4Cl\text{-}H_2O$
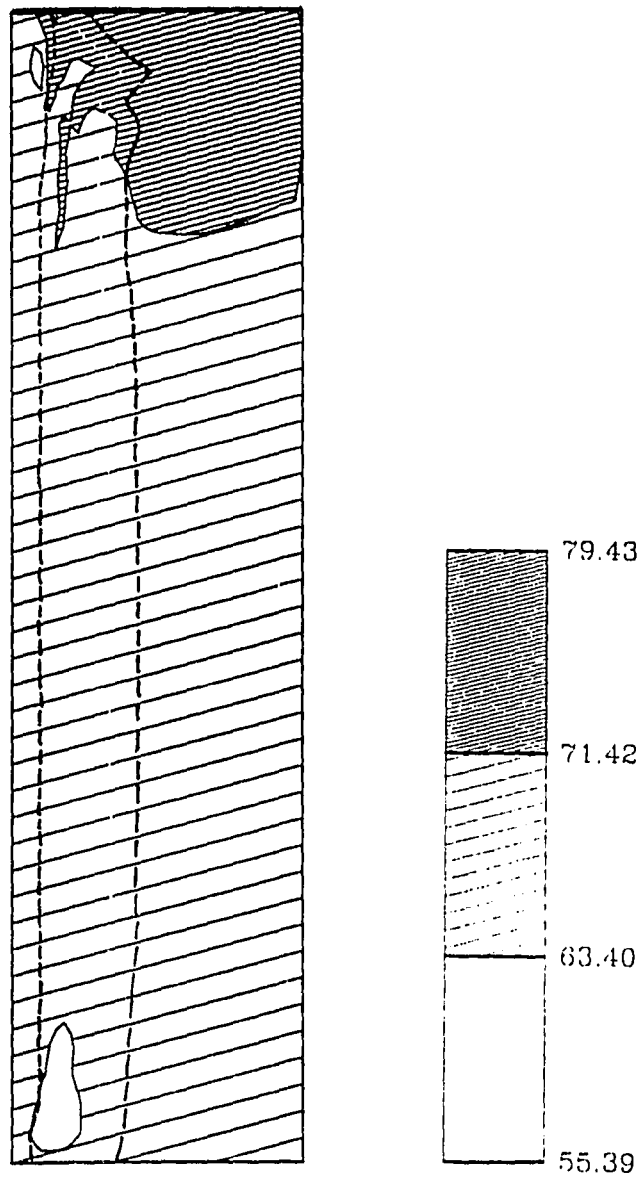
Fig. 6: Macrosegregation in horizontal solidification of
NH_4Cl-70 wt pct H_2O solution. Total concentration (in
wt pct H_2O) at t = 4 min.

(a)   (b)
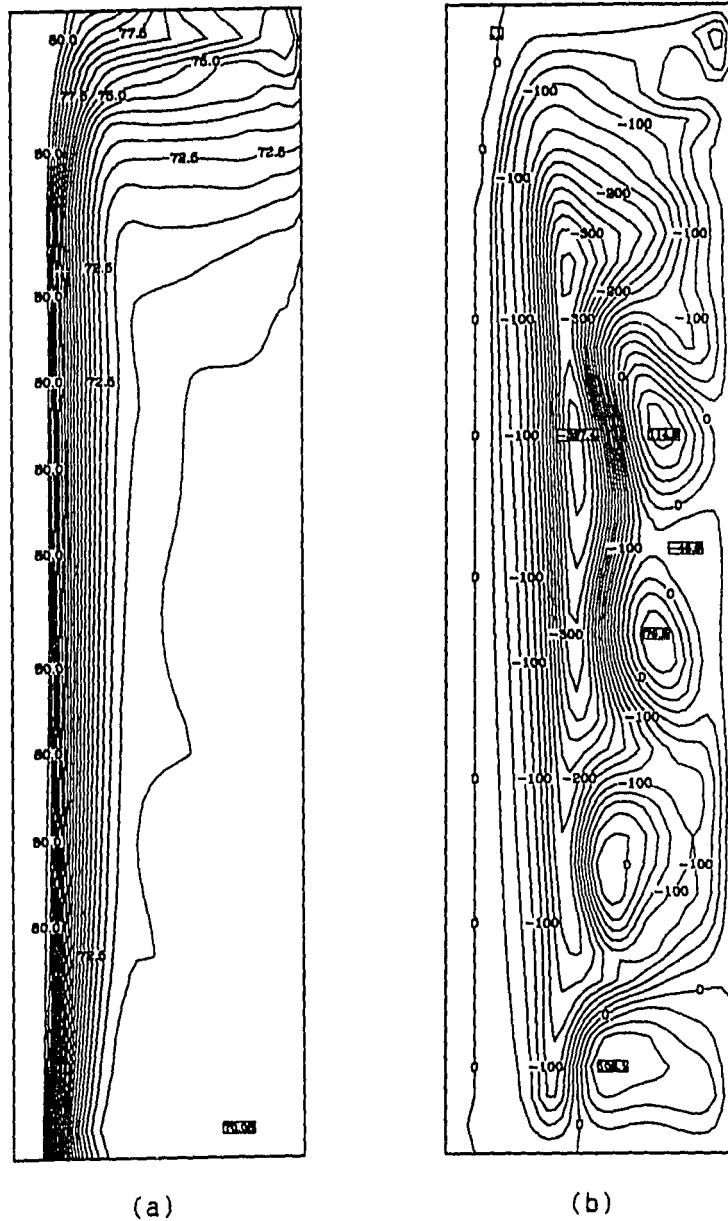
Fig. 7:   Horizontal solidification of NH_4Cl-70 wt pct H_2O
solution.   Time = 3 min. (a) Isoconcentrates in the liquid,
contours from 70.5 to 80 by 0.5 (wt pct H_2O); (b) streamlines,
contours from -375 to 100 by 25 (cm^2/s x 10^4).

system. The opposite case is observed with Pb-Sn alloys, as described in the next section.

3.2 Simulations of Freckles in Pb-Sn Alloys

After the set of test cases described in section 3.1, the code is now used to study the formation of freckles in a binary metallic alloy contained in a two-dimensional rectangular mold.

Calculations were performed for a Pb-10 wt pct Sn alloy under a variety of cooling and boundary conditions. The computational domain consisted of a rectangular region of width W and height H_T, discretized with a uniform mesh of 20 elements in the x (horizontal) direction and 30 elements in the z (vertical) direction. A uniform resolution was used because the locations of channels and regions of macrosegregation are generally unpredictable. Some of the examples were recalculated using a 40x40 mesh to verify that the results did not change significantly with the resolution of the grid. In all calculations, the channels turned out to be very narrow, comparable to one to several primary dendrite arm spacings. This scale is also comparable to the solute distribution decay scale D/V, where V is the growth rate. The mesh size has to be kept

comparable to this scale if proper resolution of the channels is desired. This requirement imposed a limitation on the size of the domain, in order not to make a single computation excessively expensive. Fortunately, all the effects associated with channel creation and growth could be observed in calculations even though the domains were rather small. Furthermore, when different mold dimensions were used, it was found that channels developed under the same thermal conditions irrespective of size of domain, an observation also made by Sarazin and Hellawell[21] in their experiments on Pb-Sn alloys.

A reference length scale $H = 300$ μm was chosen for all the calculations, which comes from the scale D/V with a growth rate $V = 10^{-2}$ mm·s^{-1} (36 mm·hr^{-1}). The following nondimensional parameters were also used:

$$Ra_T = 3.4 \times 10^{-3} \qquad Ra_s = 1.86 \times 10^4$$

$$Pr = 2.3 \times 10^{-2} \qquad Sc = 8.23 \times 10^1$$

$$L/c_s GH = 7.5 \times 10^2$$

The reference time, τ, was 0.65 s, and the reference velocity, U, was 0.27 mm·s^{-1}. The reference temperature was taken to be the freezing point of the

Pb-10 wt pct Sn alloy (T_0 = 577 K), and the reference concentration was C_0 = 10

wt pct Sn.

3.2.1 Channels Resulting from Localized Perturbations

The first calculation considers a container of width W = 10 mm with a

domain height of H_T = 20 mm. Zero tangential stress and zero vertical velocity

are imposed on the top boundary ($z = H_T$), and no-slip at the other three

boundaries. The alloy is initially all liquid of concentration C_0 = 10 wt pct Sn,

and has a linear temperature distribution varying from T_0 (the melting point)

at the bottom boundary to $T_0 + GH_T$ at the top boundary, with G = 0.1 K·m^{-1}.

The side walls are insulated, and a vertical gradient of $\partial T/\partial z = G$ is imposed

at the top boundary. A time dependent boundary condition is prescribed at

the bottom of the form:

$$T(x,0,t) = T_0 - rt$$

where r is the cooling rate (0.0783 K·s⁻¹). With this value of r, the initial

solidification rate was approximately 0.042 mm·s⁻¹. The values of the cooling

rate, r, and the thermal gradient, G, were selected from the thermal history of

ingots of Pb-10 wt pct Sn alloy that exhibited channel segregates in the

experiment of Sarazin and Hellawell.[21]

Figure 8 shows calculated results after 3 min. The contours of equal

fraction liquid (Fig. 8a) show a very narrow region of high fraction liquid at

the center of the casting, indicating the presence of a freckle or a channel.

Note that the mesh size is not sufficiently small to resolve an all-liquid jet,

because the high solidification rate gives a very small D/V scale

(approximately 70 μm). It can be seen from the streamlines (Fig. 8b) that the

flow is upward within the channel and extends into the bulk liquid as a

column of rising fluid. Although the streamlines penetrate into the mushy

zone, the strength of the convection rapidly diminishes within the mushy zone

where the permeability is low. Figure 8c shows that the fluid within the

channel is richer in solute than the surrounding fluid.

CONTOUR FROM 0.36 TO 0.96
BY 0.04

(a)

(b)

CONTOUR FROM 10.5 TO 16.25
BY 0.25

(c)
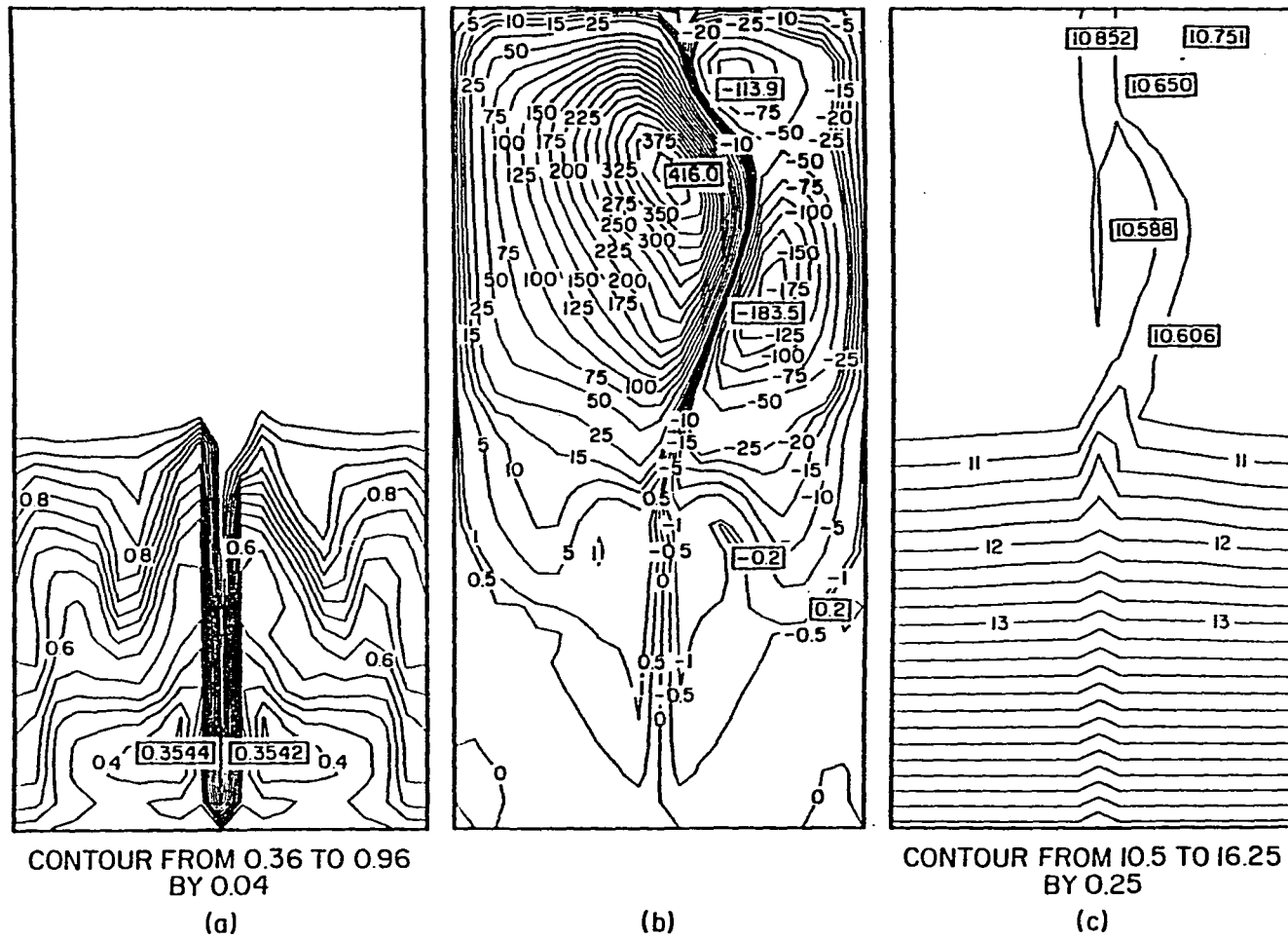
Fig. 8: Growth of a channel in the center of a Pb-Sn casting after 3 min. of solidification: (a) Fraction liquid; (b) streamlines $(cm^2/s \times 10^4)$; (c) isoconcentrates in the liquid (wt pct Sn)

A more detailed view of a freckle is obtained in the next example

(Fig. 9), where a very small container of dimensions 2.5 mm by 4.5 mm was

used, together with a slower initial solidification rate of $V = 0.0139$ mm·s^{-1}.

The width of the channel is approximately equal to the reference length scale

($H = 0.3$ mm). Note the steep gradient of fraction liquid on the channel walls,

indicating that the channel is surrounded by a region of low volume fraction

liquid. The flow is upward inside the channel (Fig. 9b), where a higher

concentration of solute is clearly observed in Fig. 9c. In addition to the two

central cells that contribute to the upward flow within the channel, two lateral

cells have developed next to the mold walls (Fig. 9b), where there is also

upward flow and a higher than normal fraction of liquid.

In the examples of Figs. 8 and 9 the channels in the centers were

induced by means of an initial perturbation in the concentration of the melt

along the vertical centerline and letting the system evolve thereafter. The form

of the perturbation was

$$C_i(\frac{W}{2},z,0) = 1.01\ C_0$$

CONTOUR FROM 0.05 TO 0.95
BY 0.05

(a)

CONTOUR FROM −3.6 TO 3.6
BY 0.4

(b)
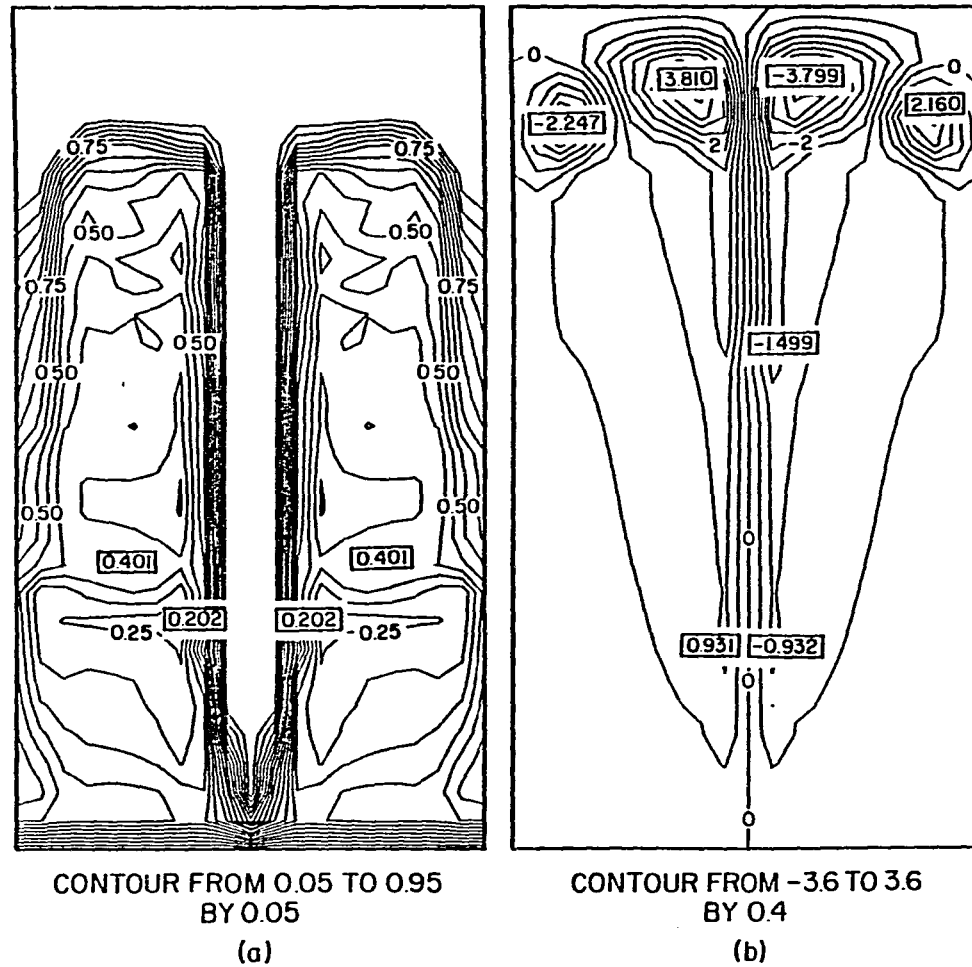
Fig. 9: Calculation in small domain showing closer details of: (a) fraction liquid; (b) streamlines at t=10 min. (cm^2/s x 10^4)

CONCENT. OF LIQUID (w%). Time =   10.00 min

CONTOUR FROM 13.9 TO 15.6 BY .1
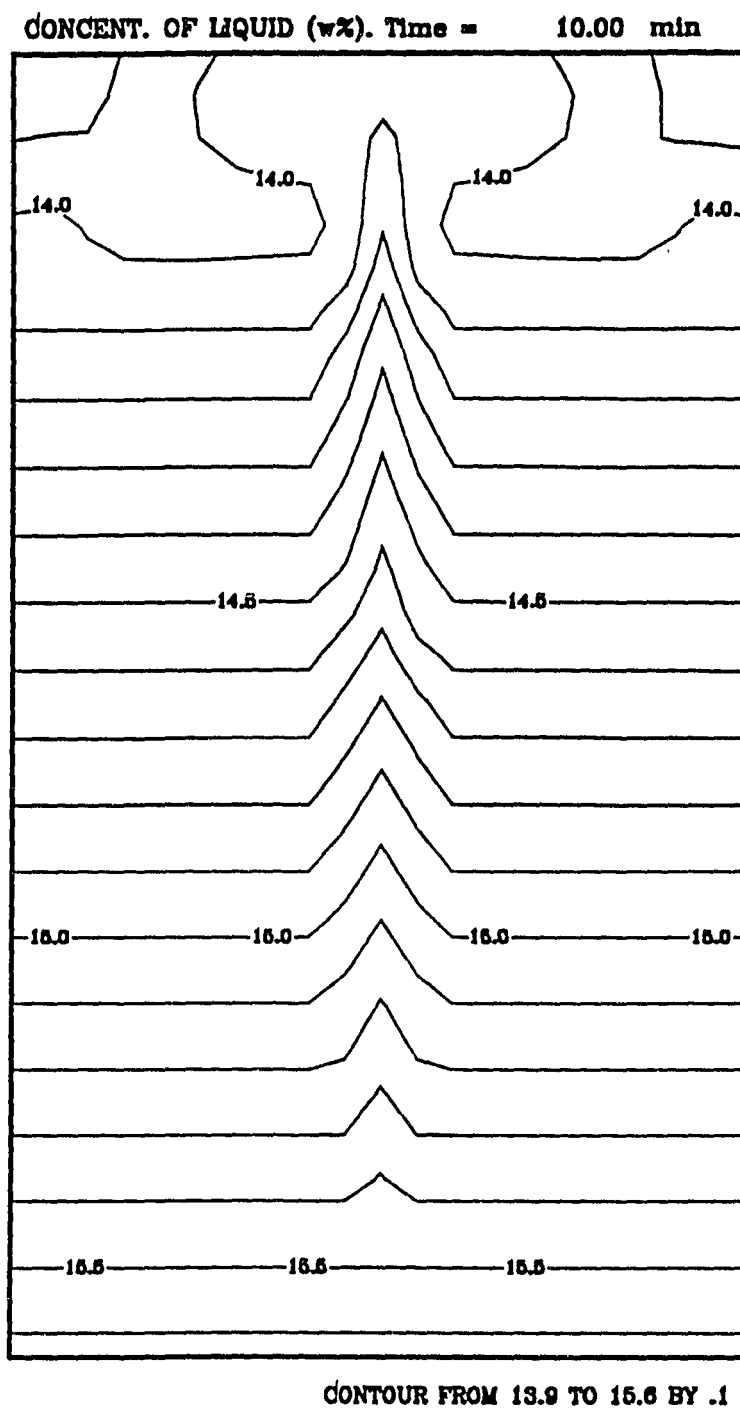
Fig. 9: (continued). (c) Isoconcentrates in the liquid (wt pct Sn).

In this way, an initial upward flow at the center of the container is established. The situation is similar to experiments done by Sample and Hellawell[7] in NH_4Cl-H_2O, in which they created channels in the mushy zone by inducing an upward flow in the liquid just ahead of the dendritic tips by suction up through a capillary tube.

3.2.2 Channels Resulting from Random Perturbations

In the next two examples, no localized perturbation is introduced. The convection is started by prescribing a random perturbation in the concentration field at the beginning of the solidification (equal to C_0), and the system is allowed to evolve undisturbed thereafter. The form of the perturbation was

$$C_l(x,z,0) = C_0(1 + 0.005\ r)$$

where $-1 \leq r \leq 1$ and r is chosen using a random number generator.

Convection also results if no perturbation is prescribed at all, because of the inherit random perturbation introduced by numerical roundoff and truncation errors. As explained in Ref. [55], however, one must explicitly provide perturbations in order to compute accurately flows of physical interest. If one relies on numerical error in order to perturb the computed solution

away from the unstable one, then the computed solution is an uncontrolled consequence of discretization and roundoff errors.

The first example shows a typical case in which freckles form on the outer surface of the solidification mold. This preference of freckles to form on the mold walls was observed in almost all the calculations performed in this study.

The alloy is initially subjected to a temperature gradient of 1 K/mm and with a linear temperature distribution varying from 577 K at the bottom to 586 K at the top. The container is 5 mm wide by 9 mm high. The side walls are insulated, and time-dependent boundary conditions are prescribed at the top and bottom of the form

$$T_{bot} = 577 - 0.00833\ t$$

$$T_{top} = 586 - 0.00833\ t$$

where temperature is in K and t is time in seconds. This yields an initial solidification rate $V = 7.77 \times 10^{-3}$ mm/s and a cooling rate close to those in the experiments of Sarazin and Hellawell[21]. The solute distribution decay scale D/V was taken as the reference length. No-stress conditions are imposed on

the velocities at the top boundary, simulating an infinitely high column of liquid above the mushy zone, and no-slip on the other three boundaries.

The calculated results in Figs. 10a, 11a, and 12a clearly display long channel-shape penetrations of liquid regions into the mushy zone along the walls of the container. The liquid in these regions is flowing upward (Figs. 10c, 11c, and 12c) and is enriched in solute (Figs. 10b, 11b, and 12b), in agreement with experimental observations. Unsuccessful attempts of channel growth are also observed in the interior of the mushy zone, resulting in closed pockets of solute-rich liquid. Although the alloy is not yet completely solidified, it is evident that the concentration of the liquid in the channels increases with time. Because a higher concentration lowers the freezing point, these regions solidify last, and produce the localized solute-rich freckles observed in the cross sections of castings.

This fact is confirmed in Fig. 13 which shows a completely solidified ingot, obtained by prescribing a zero vertical velocity at the top boundary so as to make the container finite. The cooling rate was doubled to 0.0167 K/s after 60 min of solidification, because by that time the mushy zone has reached the top of the container and the convection has greatly diminished. The alloy solidifies completely at $t = 160$ min. Figure 13 shows final composition of the casting, with evidence of strong segregation due to the channels along the

FRACTION LIQUID . Time = 5.00 min

CONCENT OF MIXTURE (w%). Time = 5.00 min

STREAM FUNCTION (X 1.E+04). Time = 5 00 m

CONTOUR FROM .5 TO .975 BY .025

CONTOUR FROM 6.75 TO 11 BY .25

CONTOUR FROM −50 TO 50 BY 0
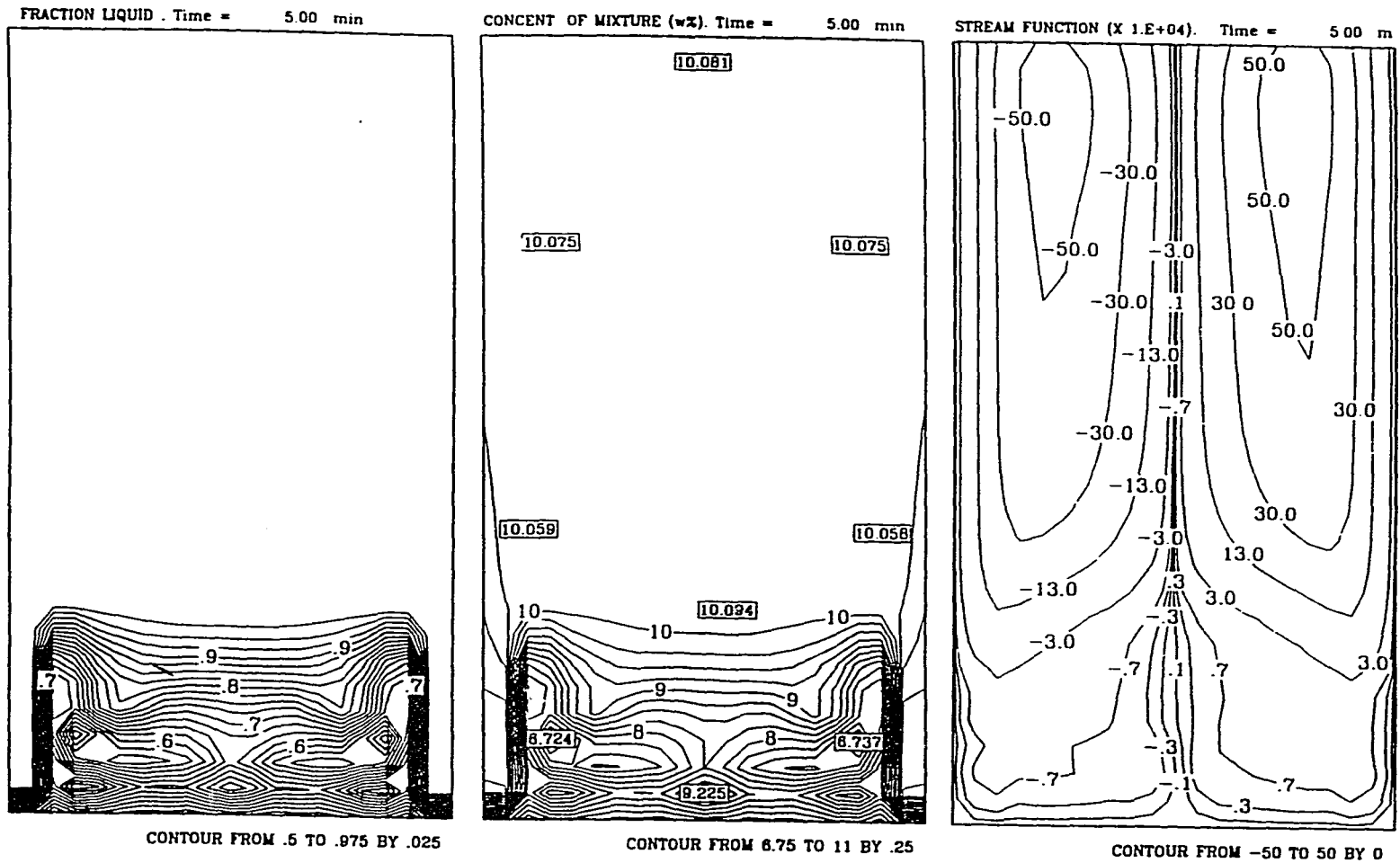
(a) Fraction liquid contours

(b) Total solute isoconcentrates

(c) Streamline contours

Fig. 10: Solidification of a Pb–10 wt pct Sn alloy at t = 5 min. (a) Fraction liquid; (b) concentration of mixture (wt pct Sn); (c) streamlines $(cm^2/s \times 10^4)$.

FRACTION LIQUID . Time = 10.00 min

CONCENT. OF MIXTURE (w%). Time = 10.00 min

STREAM FUNCTION (X 1.E+04). Time = 10.00 m

10.206   10.200

10.212

40.0

-40.0

40.0

10.212   10.219

-3.0   20.0

-.7

10

10

10

-3.0

9

.8

.8

9

9

-.7   -.1   .1   .7   3.0

7.338   7.007   8   7.232

-.3

.6

8   11   8

-.1   .1

.8

-.3   .1

8   8.701   11.398

.6   .6   .6

8   .1   .3

.6

11.782   11.786

-.3   -.1

.6   .6

8   8

.6   .6   .6   8   8.872   9   8

-.1   -.1

CONTOUR FROM .28 TO .98 BY .04

CONTOUR FROM 5.75 TO 11.75 BY .25

CONTOUR FROM -40 TO 40 BY 0
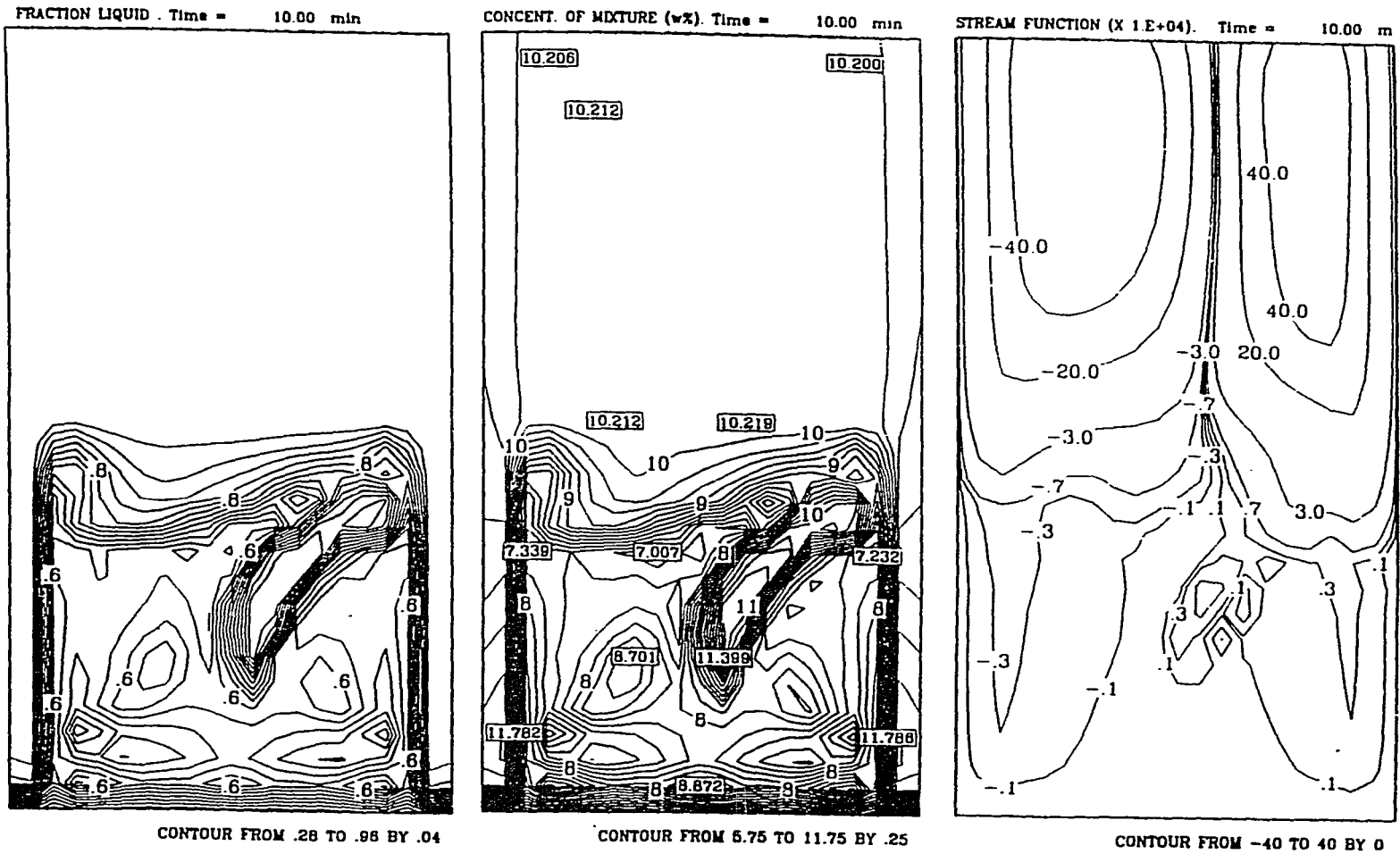
(a) Fraction liquid contours

(b) Total solute isoconcentrates

(c) Streamline contours

Fig. 11: Solidification of a Pb-10 wt pct Sn alloy at t = 10 min. (a) Fraction liquid; (b) concentration of mixture (wt pct Sn); (c) streamlines (cm^2/s x 10^4).

FRACTION LIQUID . Time = 15.00 min

CONCENT. OF MIXTURE (w%). Time = 15.00 min

STREAM FUNCTION (X 1 E+04). Time = 15.00 m

CONTOUR FROM .15 TO .95 BY .05

CONTOUR FROM 5 TO 12.5 BY .5

CONTOUR FROM −60 TO 40 BY 0

(a) Fraction liquid contours

(b) Total solute isoconcentrates

(c) Streamline contours

Fig. 12:   Solidification of a Pb-10 wt pct Sn alloy at t = 15 min. (a) Fraction liquid; (b) concentration of mixture (wt pct Sn); (c) streamlines (cm^2/s x 10^4).
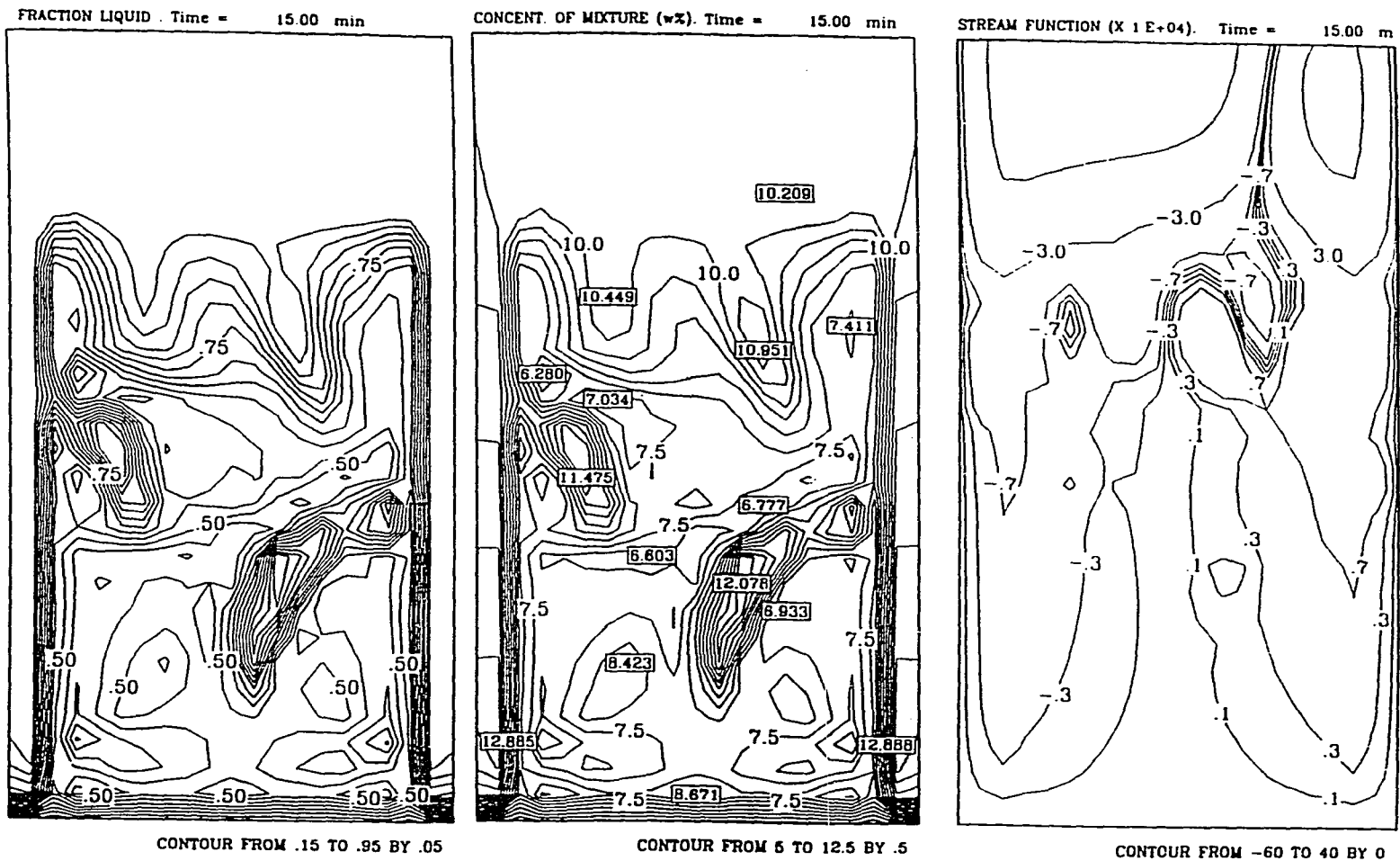
CONCENT. OF MIXTURE (w%). Time = 160.10 min
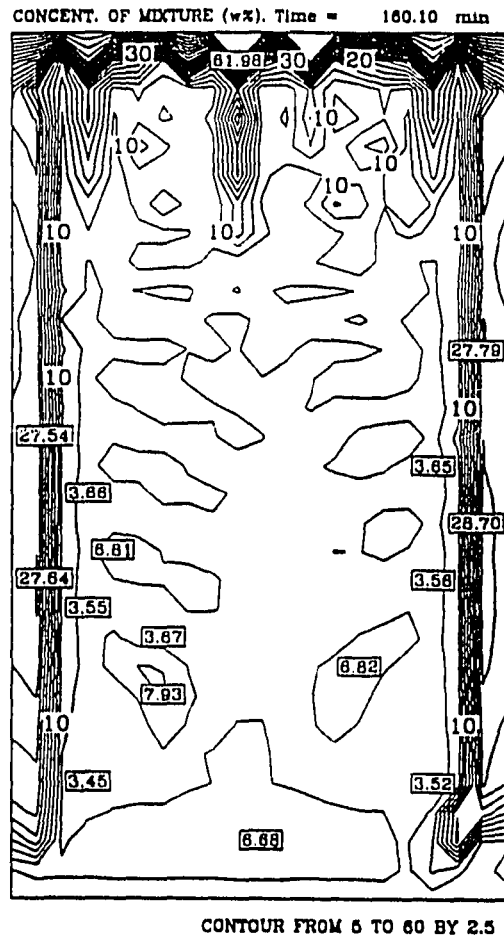
CONTOUR FROM 5 TO 60 BY 2.5

Fig. 13: Solidification of a Pb-10 wt pct Sn alloy. Final composition (wt pct Sn).

walls, where the composition has reached about 27 wt pct Sn.

Macrosegregation in the vertical direction along the interior part of the

container is also observed, with compositions varying from a depleted bottom

at about 4 wt pct Sn to a 12 wt pct Sn at the top. The pocketlike segregations

observed during solidifications have also ended with higher concentration than

the surrounding material. The strong positive segregation at the top of the

mold is due to the accumulation of buoyant solute-rich liquid in this region

during solidification. Because this is the last part of the cast to solidify, it has

a high solute content.

A similar situation results in the next example, in which a faster cooling

rate was applied, but now the channels originate in the interior of the casting

and then grow along the walls. This calculation illustrates clearly the

mechanism by which channels form. As in the previous example, the

convection is started by a random perturbation in the concentration.

The width of the mold is 5 mm, and the height of the computational

domain is $H_T = 10$ mm. No-stress conditions are imposed on the top

boundary. The cooling rate is $r = 0.0167$ K·s^{-1}, corresponding to an initial

solidification rate of $V = 0.0139$ mm·s^{-1} (50 mm·hr^{-1}). All other boundary

conditions were the same as in the examples of Figs. 8 and 9. The results are given in Figs. 14-16.

After 2 minutes into solidification, two channels begin to form (Fig. 14a) at locations corresponding to zones of upward flow of four convective cells (Fig. 15a). The negative cells in the streamline pictures indicate clockwise circulation and the positive ones, counterclockwise. The channels, however, do not keep growing upward, but they turn toward the sides and continue to grow along the walls of the mold (Figs. 14b, 14c, and 14d), following the path of upward convective flow (Figs. 15b, 15c and 15d). The convection pattern is not symmetric because the system is unstable and the perturbations are not symmetric. Even if a symmetric perturbation is prescribed, the round-off errors will deviate the convection pattern away from symmetry.

An additional channel can be seen in Fig. 14c that appears as a pocket in the upper part of the mushy zone. However, the pocket rapidly closes leaving a streak of high fraction of liquid surrounded by a dendritic network with a greater volume fraction of solid (Fig. 14d). Abrupt transitions in the volume fraction of liquid surrounding the pocket or the channels are indicated by the dark regions of closely packed contour lines.

CONTOUR FROM 0.79 TO 0.99 BY 0.01 (a)

CONTOUR FROM 0.575 TO 0.975 BY 0.025 (b)

CONTOUR FROM 0.475 TO 0.975 BY 0.025 (c)

CONTOUR FROM 0.375 TO 0.975 BY 0.025 (d)

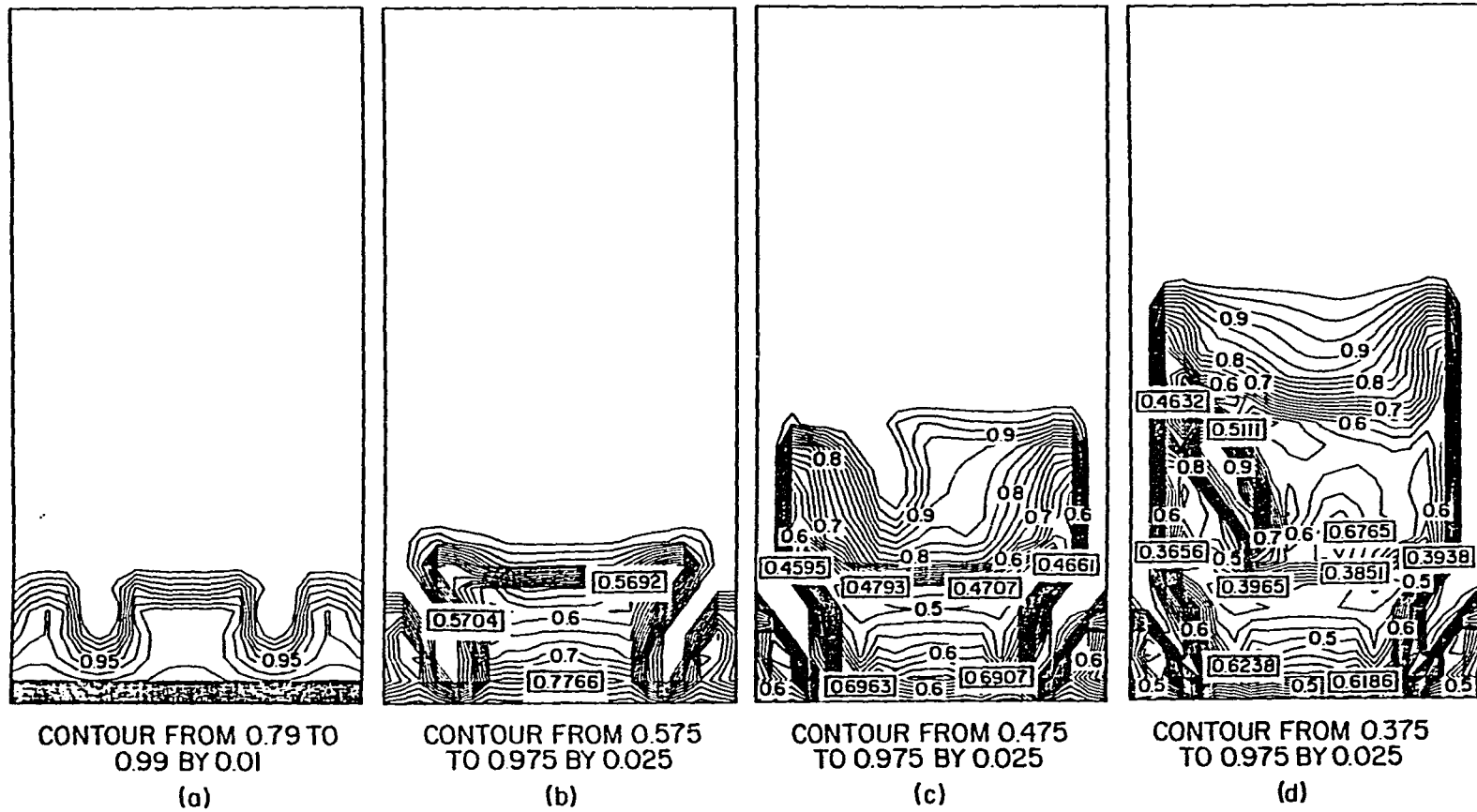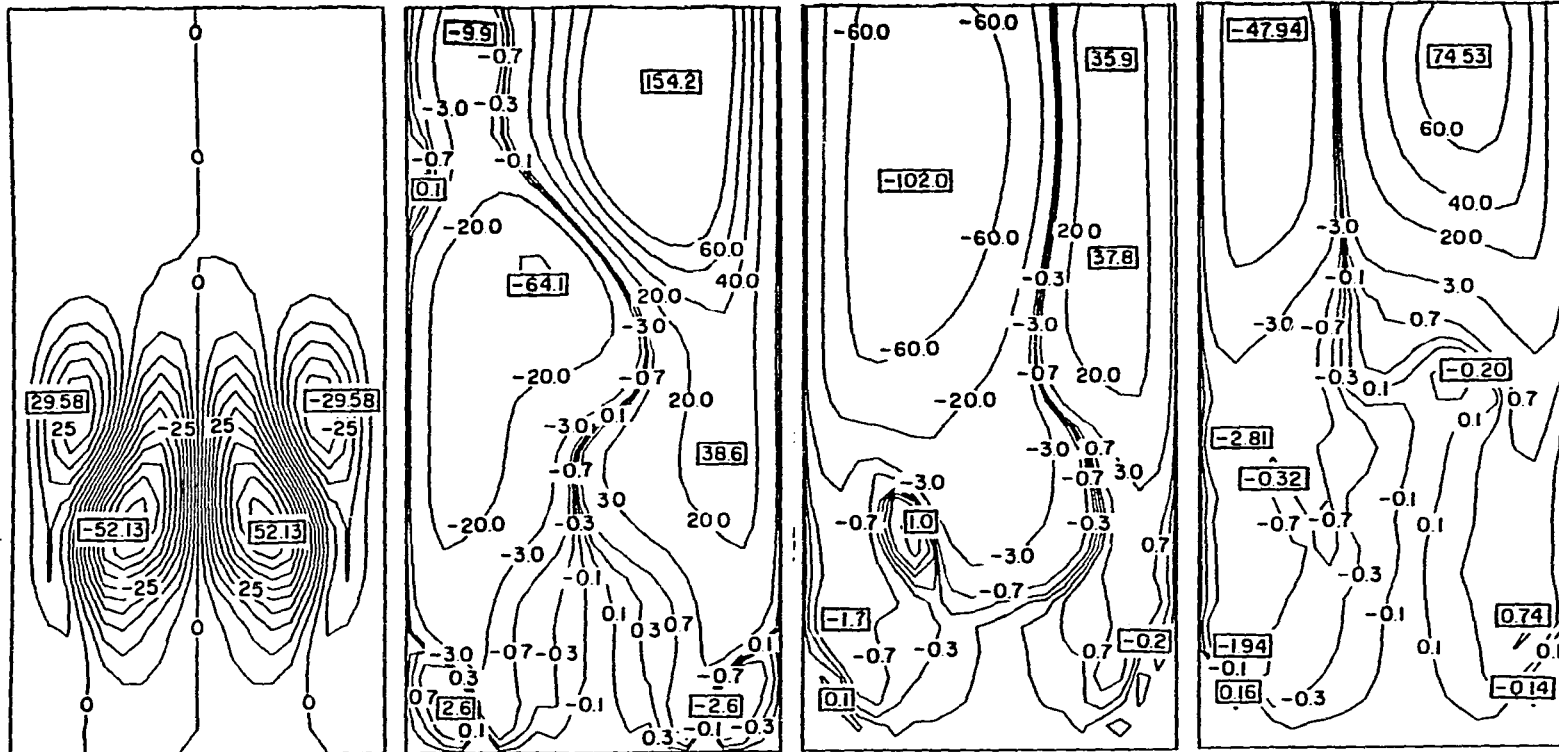Fig. 14: Formation and propagation of channels during growth of the mushy zone: Fraction liquid at (a) 2 min.; (b) 3 min.; (c) 5 min.; (d) 7 min.
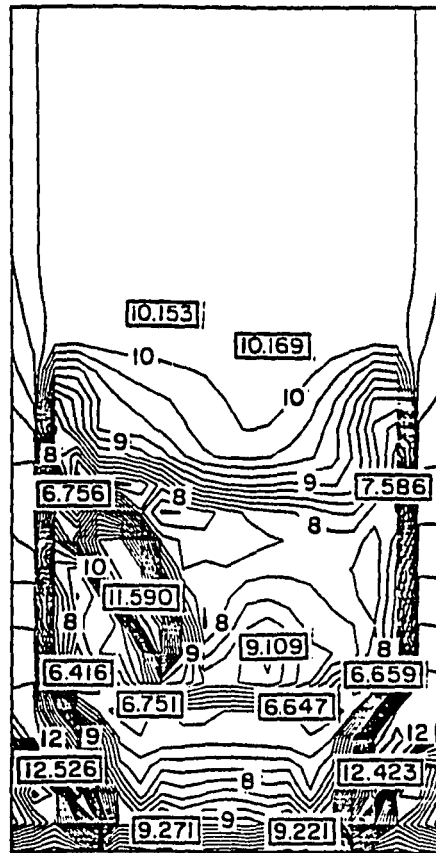
Fig. 15: Streamlines corresponding to times in Fig. 14 $(cm^2/s \times 10^4)$: (a) 2 min.; (b) 3 min.; (c) 5 min.; (d) 7 min.

CONTOUR FROM 6.5 TO 12.5
BY 0.25

Fig. 16: Total concentration (wt pct Sn) showing macrosegregation in channels, corresponding to Figs. 14d and 15d (7 min.).

A plot of total concentration of the partially solidified casting (Fig. 16) shows that within the mushy zone there is obvious positive macrosegregation in the channels along the wall and within the isolated pocket.

3.2.3 Effect of Lateral Heat Flow

The effect of heat flow between the casting and the furnace is studied in the next examples. The two calculations shown in Figs. 17a and 17b are performed in a mold of width 5 mm, with a no-stress top boundary at 10 mm, as in the previous example. The cooling rate, however, is only 8.33×10^{-3} K·s^{-1}.

In Fig. 17a heat is also extracted from the casting by imposing a temperature gradient $|\partial T/\partial x| = 0.1$ K·mm^{-1} at the side walls. Except for channels at the walls, the mushy zone adopts a concave shape toward the bulk liquid. Only channels at the walls develop and no interior channels or pockets are observed.

In Fig. 17b, heat is added to the casting by imposing $|\partial T/\partial x| = 0.3$ K·mm^{-1} at the side walls and by specifying a lower temperature (575 K) at the center of the base (increasing linearly up to 577 K toward the
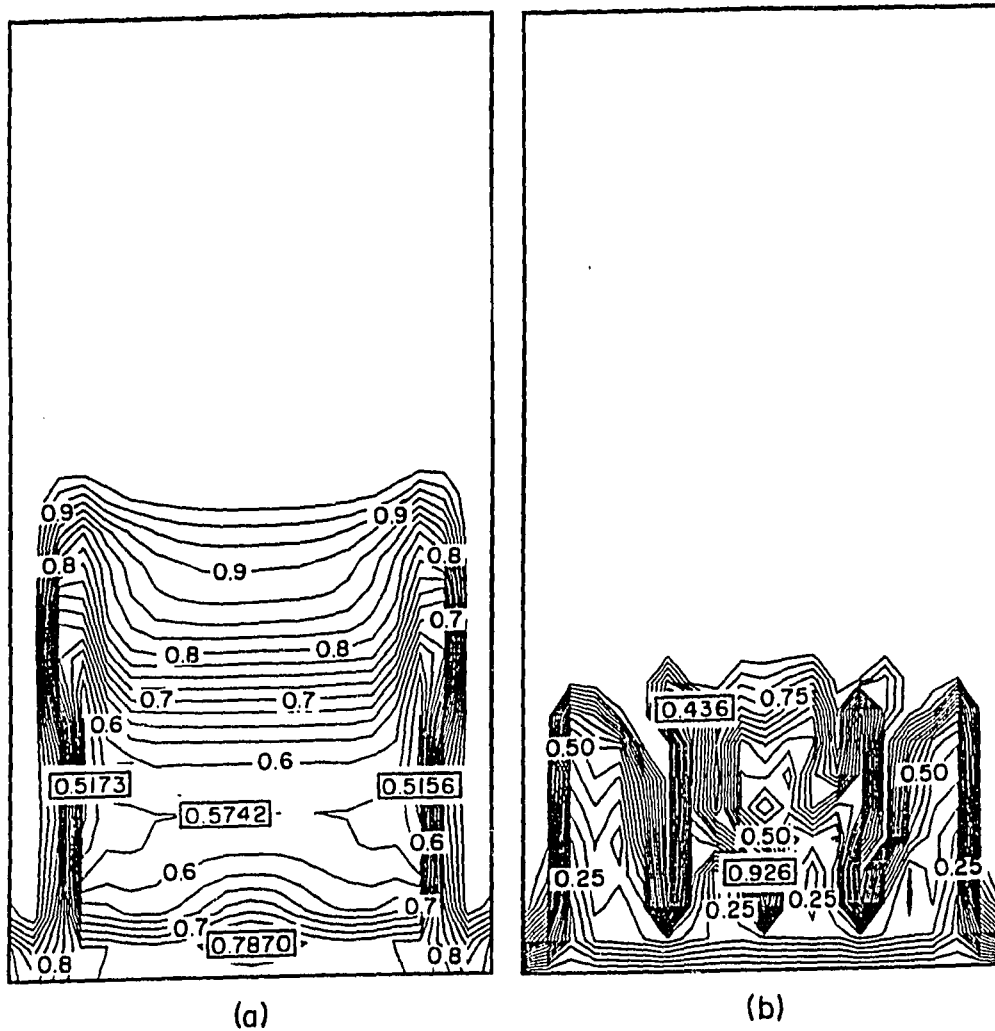
Fig. 17: Channel locations by volume fraction liquid in a: (a) concave (5 min.) mushy zone; (b) convex (20 min) mushy zone.

sides). Apart from the channels, the overall shape of the growth front is now convex to the liquid, and channels develop in the interior of the container, although the channels at the walls still remain.

Figure 18 shows a tilted mushy zone, obtained by prescribing a linear temperature profile at the bottom boundary, varying from 577 K at the left side to 580 K on the right. The side walls are insulated and the cooling rate is 1.67×10^{-2} K/s. It is observed that channels only form in the cold region (left side of the cavity).

A similar effect is observed in Fig. 19, where the container has been tilted 15 degrees to the left. This is equivalent to specifying a 15-degree deviation of the gravity vector with respect to the vertical, as shown in Fig. 19. A uniform cold temperature is applied at the bottom boundary. Observe that a channel, which originated at the bottom, tends to align with the gravity vector and then concentrates on the right, which is now the leading part of the growth front with respect to the horizontal. This phenomenon was experimentally observed by Copley et al.[5] (see their Fig. 13) in a Ni-base alloy.

It is evident from the above examples that channels tend to develop in the leading part of the growth front. This fact has also been reported in experiments with NH_4Cl-H_2O mixtures.[5,7] Copley et al.[5] varied the

FRACTION LIQUID . Time =   5.00 min

CONTOUR FROM .36 TO .96 BY .04
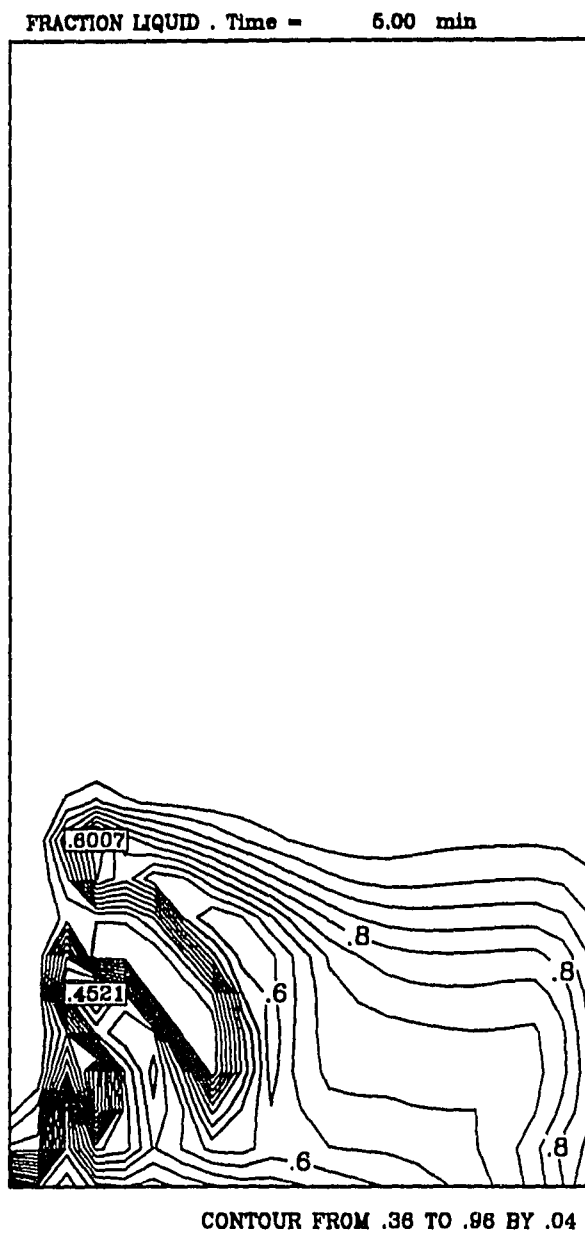
Fig. 18: Channel location in a tilted mushy zone.

FRACTION LIQUID . Time = 4.50 min

CONTOUR FROM .45 TO .975 BY .025
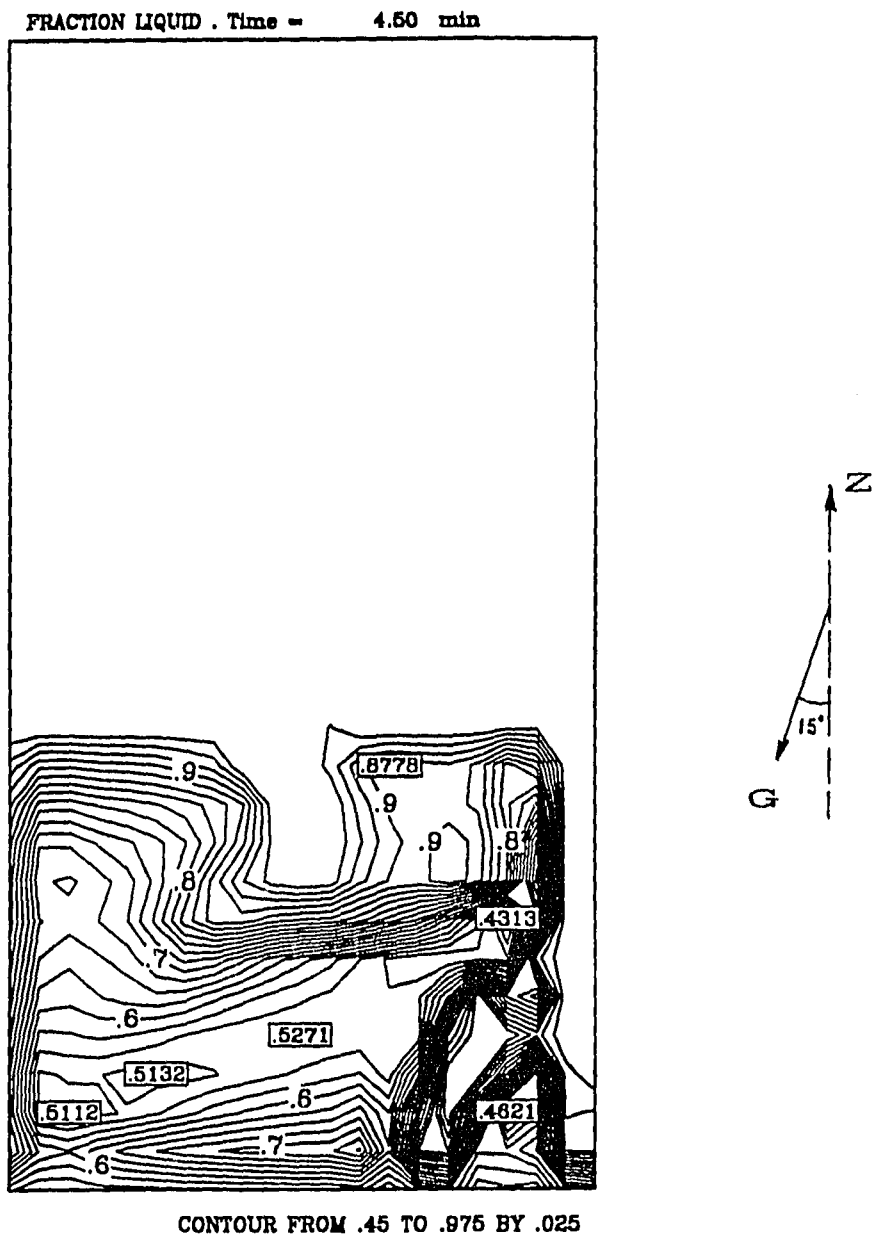
Fig. 19: Channel location in a tilted container.

configuration of their bottom chill so as to make the growth front either

concave or convex to the liquid. When it was concave, channels in the NH_4Cl-

H_2O system tended to form on the outside, and when it was convex the

channels were prevalent in the center. Similar results were obtained by

Sample and Hellawell,[71] who tilted the ingots.

3.2.4 Effect of a Localized Restriction in Horizontal

Convection

Based on the calculations presented, herein, it is evident that there is a

strong tendency for freckles to persist at the walls of the mold. In order to

investigate why the walls might be an attractive place for freckling, a

numerical experiment was done using the same domain with insulated walls

and prescribing a zero horizontal velocity along the vertical center line (i.e.

$x = W/2$). It is observed in Fig. 20a that a freckle forms at the center of the

casting and keeps growing, supported by a column of upward flowing liquid,

in a similar way as the freckles on the walls (Fig. 20b). Two additional

channels develop at positions intermediate between the center and the walls,

but they do not persist (Fig. 20c) because they face an unfavorable flow pattern

CONTOUR FROM 0.32 TO
0.96 BY 0.04

(a)

CONTOUR FROM −25 TO
25 BY 2.5

(b)

CONTOUR FROM 0.20 TO
0.95 BY 0.05

(c)

Fig. 20: Channel at the center of the casting formed by inserting a
restriction on horizontal convection: (a) contours of fraction liquid at 10
min.; (b) streamlines at 10 min. $(cm^2/s \times 10^4)$; (c) fraction liquid at 15 min.
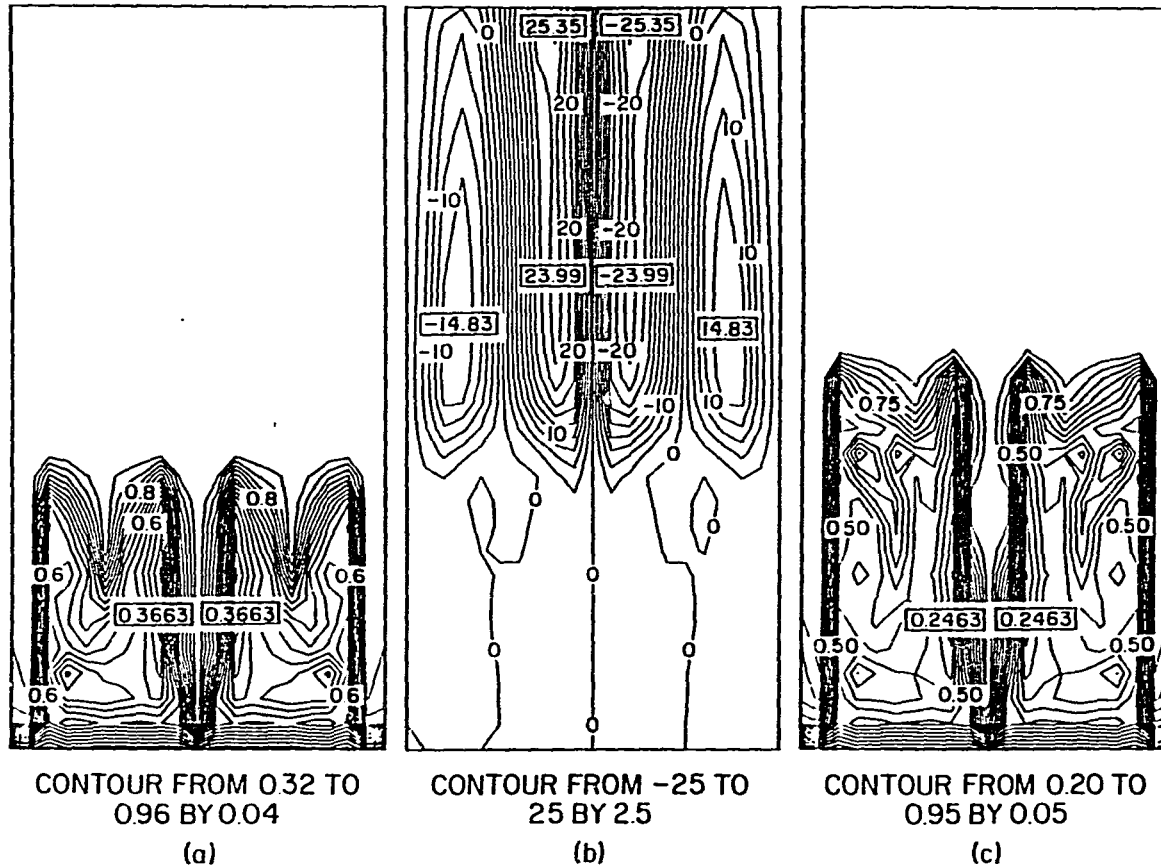
in the liquid zone. It is important to remark that in this example the upward

flow at the center of the container is not induced by an initial perturbation, but

it arises naturally as a consequence of restricting the horizontal movement of

fluid. A similar result was obtained by prescribing a highly anisotropic

permeability ($K_x = 10^{-3} K_z$) along the vertical center line in the mushy zone,

showing that a restriction to horizontal convection in the mushy zone can

sustain a column of upward flow in the liquid.

3.2.5 Horizontal Solidification of a Pb-Sn Alloy

In order to illustrate the macrosegregation pattern resulting from

horizontal solidification, a calculation was performed in a 5mm x 10mm

container with the gravity vector pointing to the right, i.e. in the x direction,

and applying a cold temperature at the boundary $z = 0$ as described in section

3.2.1. Zero vertical velocity was prescribed at $z = H_T$ and the cooling rate was

3.3×10^{-2} K/s. All other boundary conditions were the same as in section 3.2.1.

Figures 21a-d show lines of equal fraction liquid, isoconcentrates in the

liquid phase, isotherms and streamfunctions, respectively, after 5 min. of

solidification. It is observed that because of buoyancy effects, the lighter solute

FRACTION LIQUID . Time =   5.00 min
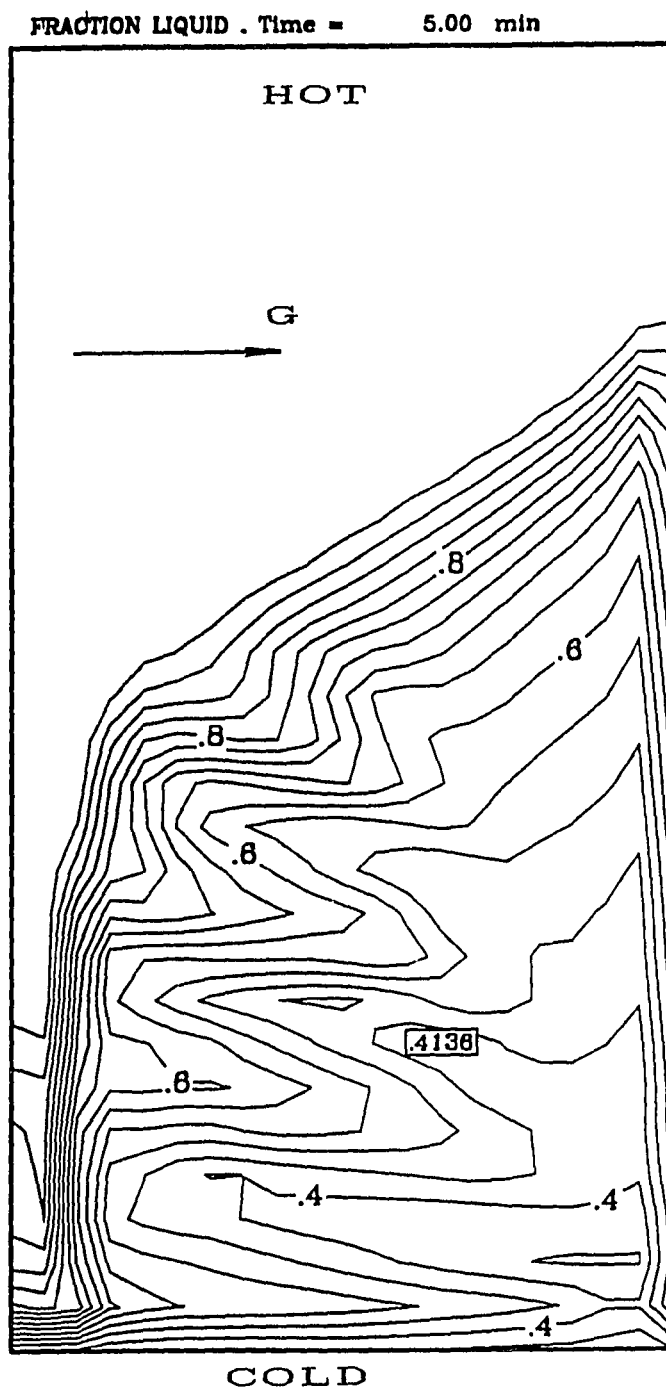
Fig. 21: Horizontal solidification of a Pb-10 wt pct Sn alloy at t = 5 min.:
(a) contours of fraction liquid

CONCENT. OF LIQUID (w%). Time = 6.00 min

11

11

12 —— 12

13 —— 13

14 —— 14
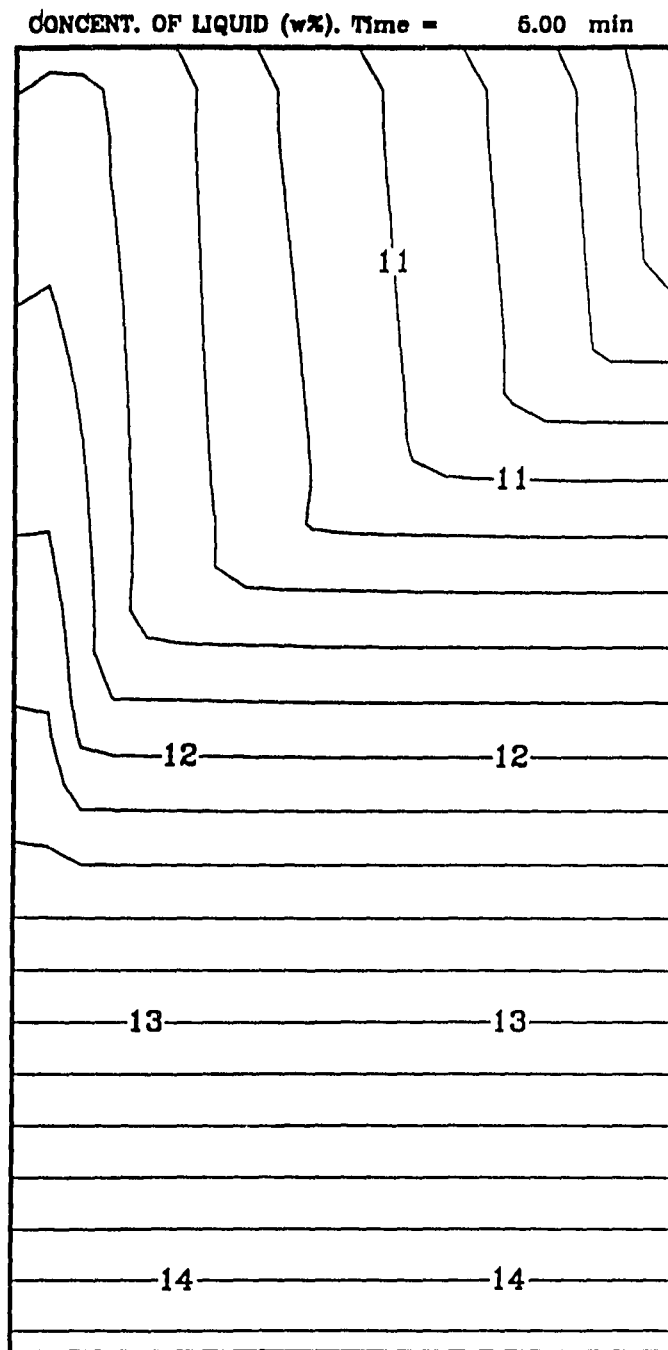
Fig. 21: (continued). (b) isoconcentrates in the liquid (wt pct Sn).

TEMPERATURE (C). Time =   5.00   min

—302.5————302.5————302.5—

—300.0————300.0————300.0—

—297.5————297.5————297.5—

Fig. 21: (continued).   (c) Isotherms (°C)

STREAM FUNCTION (X 1.E+04). Time =   5.00 m
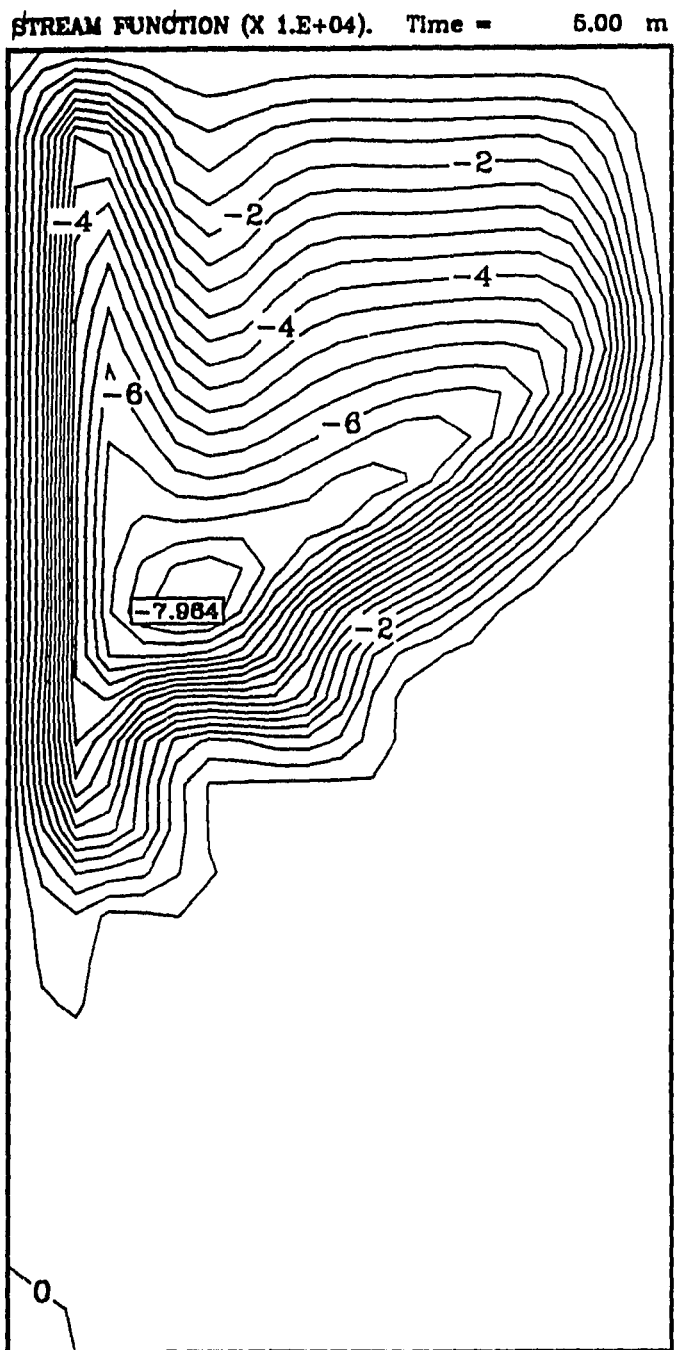
Fig. 21: (continued). (d) Streamlines (cm^2/s x 10^4)

CONCENT. OF MIXTURE (w%). Time =   65.50 min
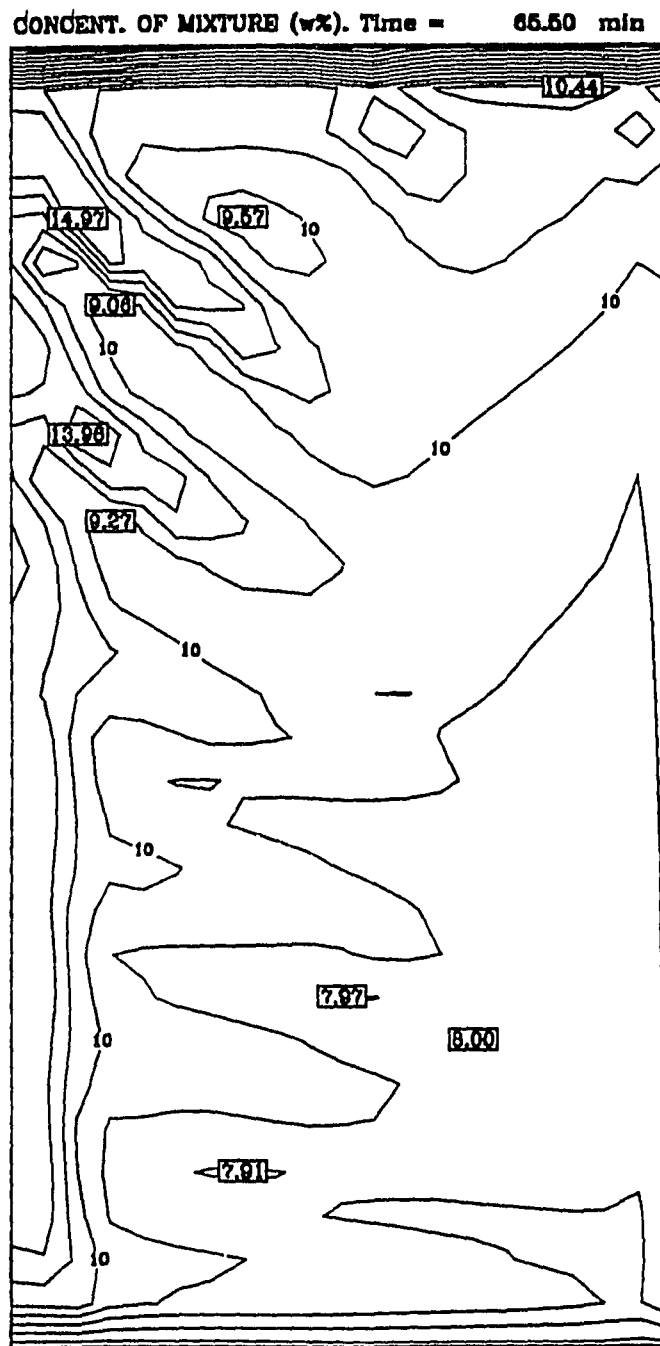
Fig. 21: (continued). (e) Final macrosegregation (wt pct Sn).

accumulates now along the top wall ($x = 0$), diminishing the freezing point in this region. The growth front then advances more rapidly along the bottom wall ($x = W$). The temperature field is practically undisturbed by the convection, which is almost entirely solute-driven. Note also that the convection in the fluid region penetrates only about 20% of the mushy zone, contrasting with the case of horizontal solidification of ammonium chloride solutions (Fig.6-7).

The predicted macrosegregation after the casting is completely solidified is shown in Fig. 21e. Note that no freckles or channels along the walls are present. Instead, "A" segregates converging to the left wall can be observed, and the macrosegregation here is not as severe as in the case of freckles. This is confirmed in Fig. 22, which shows the same ingot solidified vertically (from below), using the same cooling rate. Note that concentrations up to 30 wt pct Sn are observed along the vertical walls. The segregation is not symmetric because it depends on the history of the convection pattern, which is not symmetric. Strong segregation is also observed at the boundary $z = H_T$ of Fig. 21e, which results from the solute rejection to the liquid phase that occurred during solidification.
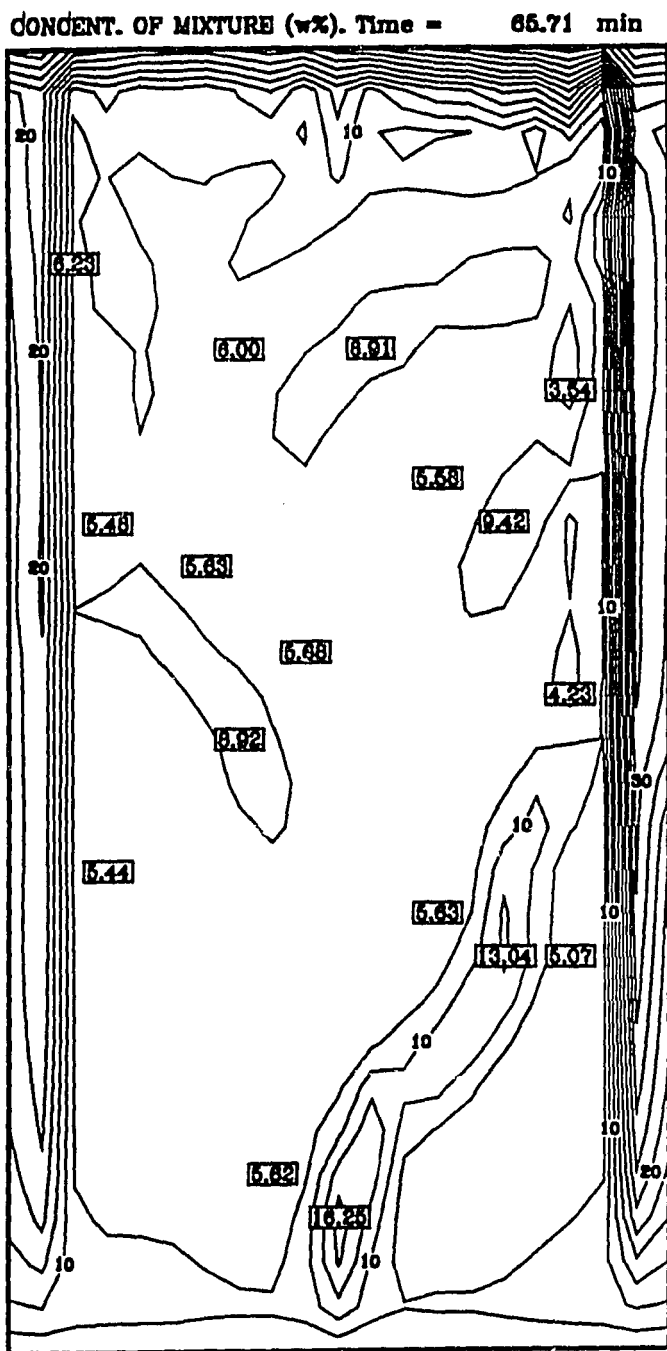
Fig. 22: Final macrosegregation (wt pct Sn) when the same casting of Fig. 21 is solidified vertically.

CHAPTER 4 - DISCUSSION

The results presented herein illustrate some of the most common effects observed in experiments on freckles. Several remarks can be made that are based upon the results.

(a)   The convection starts immediately, as soon as the liquid next to the base of the container begins to solidify. The convection cells nucleate near the advancing solidification front (i.e., at the tips of the dendrites). From the calculated temperatures and concentrations in this region, it is found that the vertical density gradient is positive there, i.e. it is gravitationally unstable.

(b)   As the solidification proceeds, the convective cells do not stay organized. The flow pattern changes continually, driven almost entirely by the solute concentration field. The isotherms are practically flat because of the low Prandtl number. In the Pb-10 wt pct Sn alloy, the convection in the bulk liquid penetrates deeply into the mushy zone, although the velocities decrease by 2 or 3 orders of magnitude below

the upper 20 pct of the mushy zone. On the other hand, strong convection is observed in the mushy zone of the ammonium chloride system, due to the relatively high permeability (approximately 80% of liquid at eutectic, compared with 7% in Pb-10wt pct Sn).

(c)   The first channels begin to form in regions of upward flow, between two convective cells (Figs. 14a and 15a). Because the solute concentration in the liquid is higher at the bottom of the casting, the upward flow transports solute-rich liquid to the tips of the dendrites, decreasing the freezing point. Therefore, the growth front advances more slowly in regions where there is upward flow, it distorts, and a channel begins to develop backward from the tips toward the bottom of the mushy zone. This process is helped further by remelting of already existing solid in the mushy zone. The diffusion of solute is too slow to spread away from the column of rising solute-rich liquid, so remelting occurs in order to decrease the solute concentration in the liquid back to an equilibrium value that corresponds to the local temperature. In other words, without remelting a volume of rising interdendritic liquid is unable to maintain its thermodynamic equilibrium because heat diffuses much faster than the solute; remelting counteracts this by diluting the liquid with respect to the solute.

(d)   The larger concentration of solute in a column of rising liquid tends to

keep it rising because of buoyancy and double diffusion effects

(assuming that the solute is lighter than the solvent). This keeps the

channel growing vertically, until the pattern of convection changes, and

the column of liquid emerging from the channel is disturbed. The flow

change is caused by accumulation of solute in a nearby place, creating a

competing channel. The old channel deviates from its vertical trajectory,

induced by the upward flow at the new position, and eventually merges

with the new channel or closes before reaching it, forming a pocket or

streak.

(e)   In most of our calculations, we observe a strong accumulation of solute

at the walls of the mold, leading to long, well defined channels that

dominate the flow and prevent other similar channels from growing in

the interior of the casting. Channels that develop in the interior of the

casting, either naturally or induced by a perturbation, are eventually

absorbed by the channels at the walls. This predominance of freckling

at the surface of the mold has been observed in Ni-based alloys[9].

Freckling at the walls has also been reported in Pb-Sn alloys[22] in small

width containers like the ones used in this study. The solute

accumulates next to the walls because of the limitation of lateral

transport; i.e. it is harder to remove solute away from the wall because the horizontal component of the velocity is small. For high solidification rates (~4.2 mm·s^{-1}) the formation of channels at the walls can be delayed or prevented, because not enough time is allowed for solute accumulation (Figs. 8 and 9).

(f)   Long, vertical channels, similar to the ones at the surface of the casting, can be obtained in the interior if a restriction to lateral convection is introduced (Fig. 20). The purpose is to provoke an accumulation of solute that can sustain the channel growth. Such an accumulation could occur in regions of high anisotropy in the mushy zone ($K_x < K_z$), as might be the case in grain boundaries, dendrite misalignments or other defects in the dendritic network of the mushy zone. Another mechanism that can favor the formation of long interior channels is the deposit of dendrite debris, produced by remelting or erosion of the dendrite arms, along the channel sides. This phenomenon has been visualized in the NH_4Cl-H_2O system.[5] The debris grow as small randomly oriented grains that entangle with the sides of the channel and reduce the horizontal permeability. In effect, the solute is confined to the channel. Because this decreases the lateral feeding of liquid, the channel activity is significant only in the neighborhood of the dendrite

tips, and the liquid in the bottom part of the channel is essentially stagnant.

(g) The position where channels form within the casting, can be affected by heat flow at the vertical walls (Fig. 17), by the thermal profile of the base chill (Fig. 18), and by tilting the solidification mold (Fig. 19). In all cases, the same physical phenomenon is involved: solute-driven buoyancy convection. Cold regions of the mushy zone are solute-rich because of the thermodynamic constraint imposed by the equilibrium phase diagram. Because the solute (Sn in the Pb-Sn alloy, and water in the NH_4Cl-H_2O system) is lighter than the solvent, these regions will originate upward fluid flow, which in turn attracts more solute-rich fluid from the bottom part of the mushy zone. That is why, during solidification, channels tend to follow the leading part of the mushy zone, i.e. the cold regions where more advanced growth has occurred.

(h) By comparing completely solidified castings, it is found that the localized macrosegregation in freckles of an alloy that has been solidified vertically (Fig. 22), is more severe than the segregation in the "A" segregates of an alloy solidified horizontally (Fig. 21e). This is another proof of the role of buoyancy effects in final segregation. As mentioned in point (g), vertical solidification from below attracts solute-

rich fluid from the bottom of the mushy zone, while this is not the case

in horizontal solidification, in which the resulting segregation is less

severe.

CHAPTER 5 - SUMMARY AND FUTURE WORK

A mathematical model of solidification of dendritic alloys with thermosolutal convection has been presented. The solidification is initiated from an all-liquid state, and the dendritic zone is allowed to grow as the volume fraction of liquid in the mushy zone adjusts according to local thermodynamic equilibrium conditions. Calculations were performed for the directional solidification of a Pb-10 wt pct Sn alloy, with the following results:

(a)   Channels form during the growth of the mushy zone.

(b)   The shape of the channels vary from small pockets or short streaks of interdendritic liquid to long vertical penetrations.

(c)   The position where channels form within the casting tend to follow the leading part of the growth front.

(d)   The liquid within the channels is enriched in solute, resulting in strong segregation after complete solidification.

(e)   The channels form in regions of upward flow. The mushy zone

        grows around the columns of rising liquid, forming the channels

        backward from the tips of the dendrites toward the bottom of the

        mushy zone. Remelting also takes place.

(f)   The convection is driven mainly by the solute field. Zones of

        solute accumulation are potential starters of channels.

(g)   Channels can be induced by establishing a column of upward

        flow in the bulk liquid, by introducing a restriction to the

        horizontal convection in the mushy zone, or by enhancing the

        vertical convection.

(h)   There is a strong preference for channels to form at the mold

        walls.

(i)   It is difficult to sustain long, vertical channels in the interior of

        the casting. A mechanism is proposed that can lead to such types

        of channels.

(j)   When the alloy is solidified horizontally, "A"-type segregates

form instead of freckles. The localized segregation in these

defects is less severe than in the case of freckles.

(k)   Numerical prediction of freckles is computationally expensive,

imposing a limitation in the size of the calculation domain.

The model presented in this study successfully predicts, for the first

time, many of the qualitative features of freckle formation observed in

experiments of vertical solidification of binary metallic alloys. It also simulates

"A"-type segregation in horizontal solidification of metallic and non-metallic

alloys, again in agreement with reported observations and the calculations of

other investigators. Although computed values of freckle diameter and

composition fall within the range of reported experimental results (e.g. 200 -

1200 μm freckle diameter[21,22,54] and 13.5 wt pct Sn composition during

solidification of Pb-10 wt pct Sn[54]), the exact simulation of a real experimental

setting is severely limited by the high computational cost of resolving the

small scales associated with freckles, in the large solidification molds that are

utilized in practice. A calculation in a small domain of dimensions 1 cm x 2

cm, with a 40 x 40 mesh, requires approximately 2 hours of CPU time in a

Cray Y/MP8 per hour of solidification. The simulation of freckles in Sarazin

and Hellawell's experiments[21] for example, with container dimensions of 4 cm

(diameter) x 12 cm, would be prohibitively expensive. Furthermore, close quantitative predictions may require the use of 3-D models and a more general treatment of transport aspects, based on properly characterized thermophysical properties. An adaptive grid method, that automatically refines the mesh in locations where freckles and segregation regions form, could save both memory and CPU time costs. Parallel computing in the new massive parallel machines, with computational speeds approaching the teraflop range, is seen as the most attractive alternative to model 3-D problems.

APPENDIX

FUNCTIONS USED FOR PERMEABILITY

We assume directional solidification with dendritic columnar grains. The permeability is anisotropic with components K_x and K_y for flow perpendicular to the columnar dendrites and flow parallel to the columnar dendrites, respectively.

In this work thermal conditions, corresponding to ingots studied by Sarazin and Hellawell,[21] were used in the simulations, so we also used their reported primary dendrite arm spacing of 300 μm. Lacking a value for secondary dendrite arm spacing, Eq. [30] of Reference [35] was selected for K_x; it is

$$K_x = 7.08 \times 10^{-16} \, d_1^{2.08} \, \phi^{3.32} \qquad [A1]$$

with K_x and m^2 and d_1 in μm.

Equation [A1] is based on a regression analysis of empirical data that cover the scope $0.19 \leq \phi \leq 0.66$ and $144 \leq d_1 \leq 420$ μm.

For the regime with $\phi > 0.66$, we use

$$\frac{K_x}{d_1^2} = a_0 + a_1\left(\frac{\phi}{1-\phi}\right)^{1/4} \qquad \text{[A2]}$$

where

$a_0 = -5.955449 \times 10^{-2}$

$a_1 = 5.652925 \times 10^{-2}.$

Equation [A2] and the coefficients were determined by a linear regression of results given in Tables 1 and 2 of Sangani and Acrivos[47] for $0.6 \leq \phi < 0.95$, and calculated with their Eqs. (17) and (25) for $0.95 \leq \phi \leq 0.99$. Sangani and Acrivos[47] studied the slow flow past square arrays and triangular arrays of circular cylinders; Eq. [A2] is a compromise between the square array and the triangular array.

Flow Parallel to Columnar Dendrites

The empirical data are listed in Reference [35]; the scope is $0.17 \leq \phi \leq 0.61$ and $28 \leq d_1 \leq 420$ µm for which the following empirical relationship was determined:

$$\frac{K_z}{d_1^2} = 3.75 \times 10^{-4}\ \phi^2 \qquad \text{[A3]}$$

There are no empirical data for $\phi > 0.61$, so we use the results of Drummond and Tahir[48] and Ganesan.[36]

Drummond and Tahir derived equations for laminar flow parallel to regular arrays of circular cylinders. Based upon values of drag forces given in their Table 5 and their equations for small values of $(1 - \phi)$, permeabilities were calculated.

Ganesan[36] calculated the permeability for flows parallel to primary dendrites based upon actual microstructures. His results agree very well with the results derived from Drummond and Tahir for $g_L \geq 0.55$. Therefore, when $\phi > 0.61$ we use an equation given by them; it is

$$\frac{K_z}{d_1^2} = a\left[\ln (1 - \phi)^{-1} - b + 2(1 - \phi) - \frac{(1 - \phi)^2}{2} \right] \qquad \text{[A4]}$$

where a and b are constants that depend on the array of the cylinders. In this work, we selected average values for triangular and square arrays:

$a = 0.07425$

$b = 1.487$.

REFERENCES

1. M. McLean: *Directionally Solidified Materials for High Temperature Service*, The Metals Society, 1983, London, pp. 1-8.

2. V. Laxmanan, A. Studer, L. Wang, J. F. Wallace and E. A. Winsa: NASA Technical Memorandum 89885, presented at the Low Gravity Science Seminar Series, University of Colorado, Boulder, CO, Feb. 17, 1986.

3. R. J. McDonald and J. D. Hunt: *Trans. TMS-AIME*, 1969, vol. 245, pp. 1993-97.

4. R. J. McDonald and J. D. Hunt: *Metall. Trans.*, 1970, vol. 1, pp. 1787-88.

5. S. M. Copley, A. F. Giamei, S. M. Johnson and M. F. Hornbecker: *Metall. Trans.*, 1970, vol. 1, pp. 2193-2204.

6. A. K. Sample and A. Hellawell: *Metall. Trans. B*, 1982, vol. 13B, pp. 495-501.

7. A. K. Sample and A. Hellawell: *Metall. Trans. A*, 1984, vol. 15A, pp. 2163-73.

8. C. F. Chen and F. Chen: *J. Fluid Mech.*, accepted for publication.

9. A. F. Giamei and B. H. Kear: *Metall. Trans.*, 1970, vol. 1, pp. 2185-91.

10. R. Mehrabian, M. A. Keane and M. C. Flemings: *Metall. Trans.*, 1970, vol. 1, pp. 3238-41.

11. N. Standish: *Metall. Trans.*, 1970, vol. 1, pp. 2026-27.

12. N. Streat and F. Weinberg: *Metall. Trans.*, 1972, vol. 3, pp. 3181-84.

13. M. J. Stewart and F. Weinberg: *J. Crys. Growth*, 1972, vol. 12, pp. 217-27.

14. P. Nandapurkar, D. R. Poirier, J. C. Heinrich and S. Felicelli: *Metall. Trans. B*, 1989, vol. 20B, pp. 711-21.

15. J. C. Heinrich, S. Felicelli, P. Nandapurkar and D. R. Poirier: *Metall. Trans. B*, 1989, vol. 20B, pp. 883-91.

16. J. C. Heinrich, S. Felicelli and D. R. Poirier: *Comp. Meth. Appl. Mech. Eng.*, 1991, to be published.

17. S. Kou, D. R. Poirier and M. C. Flemings: *AIME Electric Furnace Conference Proceedings*, 1977, pp. 221-228.

18. S. Kou, D. R. Poirier and M. C. Flemings: *Metall. Trans. B*, 1978, vol. 9B, pp. 711-19.

19. S. D. Ridder, F. C. Reyes, S. Chakrovorty, R. Mehrabian, J. D. Nauman, J. H. Chen, and H. J. Klein: *Metall. Trans. B*, 1978, vol. 9B, pp. 415-425.

20. S. D. Ridder, S. Kou, and R. Mehrabian: *Metall. Trans. B*, 1981, vol. 12B, pp. 435-47.

21. J. R. Sarazin and A. Hellawell: *Metall. Trans. A*, 1988, vol. 19A, pp. 1861-71.

22. S. N. Tewari and R. Shah: *Metall. Trans. A*, accepted for publication.

23. M. C. Flemings and G. E. Nereo: *Trans. TMS-AIME*, 1968, vol. 242, pp. 50-55.

24. J. Verhoeven: *Metall. Trans.*, 1971, vol. 2, pp. 1673-1680.

25. W. D. Bennon and F. P. Incropera: *Int. J. Heat Mass Transfer*, 1987, vol. 30, pp. 2161-70.

26. W. D. Bennon and F. P. Incropera: *Int. J. Heat Mass Transfer*, 1987, vol. 30, pp. 2171-87.

27. W. D. Bennon and F. P. Incropera: *Metall. Trans. B*, 1987, vol. 18B, pp. 611-16.

28. W. D. Bennon and F. P. Incropera: *Num. Heat Transfer*, 1988, vol. 13, pp. 277-96.

29. C. Beckermann and R. Viskanta: *Physico Chem. Hydrodyn.*, 1988, vol. 10, pp. 195-213.

30. C. Beckermann and R. Viskanta: *Int. J. Heat Mass Transfer*, 1988, vol. 31, pp.35-46.

31. A. C. Fowler: *IMA J. Appl. Math.*, 1985, vol. 35, pp. 159-74.

32. M. Simpson, M. Yerebakan and M. C. Flemings: *Metall. Trans. A*, 1985, vol. 16A, pp. 1687-89.

33. L. H. Shaw, J. Beech and R. H. Hickley: *Ironmaking and Steelmaking*, 1986, vol. 13, pp. 154-60.

34. S. Ganesan and D. R. Poirier: *Metall. Trans. B*, 1990, vol. 21B, pp. 163-81.

35. D. R. Poirier: *Metall. Trans. B*, 1987, vol. 18B, pp. 245-55.

36. S. Ganesan: Ph.D. dissertation, University of Arizona, Tucson, AZ, 1990.

37. P. J. Nandapurkar, D. R. Poirier and J. C. Heinrich: *Num. Heat Transfer*, Part A, 1991, vol. 19, pp. 297-311.

38. D. R. Poirier, P. J. Nandapurkar and S. Ganesan: *Metall. Trans. B*, 1991, vol. 22B, to be published.

39. M. C. Flemings: *Solidification Processing*, McGraw-Hill Book Co., New York, NY, 1974, pp. 141-46.

40. *Metals Handbook*, 8th ed., ASM, Metals Park, OH, 1973, vol. 8, p. 330.

41. D. R. Poirier: *Metall. Trans. A*, 1988, vol. 19A, pp. 2349-54.

42. H. R. Thresh and A. F. Crawley: *Metall. Trans.*, 1970, vol. 1, pp. 1531-35.

43. D. R. Poirier and P. Nandapurkar: *Metall. Trans. A*, 1988, vol. 19A, pp. 3057-61.

44. J. C. Heinrich: *Comp. Meth. Appl. Mech. Engng.*, 1988, vol. 69, pp. 65-88.

45. J. C. Heinrich: *Int. J. Num. Meth. Engng.*, 1984, vol. 20, pp. 447-64.

46. M. C. Flemings and G. E. Nereo: *Trans. TMS-AIME*, 1967, vol.239, pp. 1449-61.

47. A. S. Sangani and A. Acrivos: *Int. J. Multiphase Flow*, 1982, vol. 8, pp. 193-206.

48. J. E. Drummond and M. I. Tahir: *Int. J. Multiphase Flow*, 1984, vol. 10, pp. 515-40.

49. T. Fuji, D. R. Poirier, and M. C. Flemings: *Metall. Trans. B*, 1979, vol 10, pp. 331-39.

50. A. L. Maples and D. R. Poirier: *Metall. Trans. B*, 1984, vol. 15, pp. 163-72.

51. F. Kaempffer and F. Weinberg: *Metall. Trans.*, 1971, vol. 2, pp. 3051-54.

52. G. H. Geiger and D. R. Poirier: *Transport Phenomena in Metallurgy*, 1973, Addison-Wesley, Reading, Massachusets, pp. 336-339.

53. J. Szekely and A.S. Jassal: *Metall. Trans. B*, 1978, vol. 9B, pp.389-98.

54. J. R. Sarazin and A. Hellawell: *EPD Congress '91*; D. R Gaskell, editor; The Mineral, Metals & Materials Society, 1991, pp. 511-522.

55. C.R. Anderson, C. Greengard, L. Greengard, and V. Rokhlin: *Phys. Fluids A*, 1990, vol. 2, pp. 883-885.